

# Earth Matter Effects at Very Long Baselines and the Neutrino Mass Hierarchy

---

Raj Gandhi, Pomita Ghoshal, Subabati Goswami, Poonam Mehta<sup>x</sup>

Harish-Chandra Research Institute,  
Chhatnag Road, Jhansi,  
Allahabad 211 019, India

S Uma Sankar<sup>d</sup>

Department of Physics,  
I. I. T., Powai,  
Mumbai 400 076, India.

**Abstract:** We study matter effects which arise in the muon neutrino oscillation and survival probabilities relevant to atmospheric neutrino and very long baseline ( $> 4000$  Km) beam experiments. The inter-relations between the three probabilities  $P_{e\mu}$ ,  $P_{e\tau}$  and  $P_{\mu\tau}$  are examined. It is shown that large and observable sensitivity to the neutrino mass hierarchy can be present in  $P_{\mu\tau}$  and  $P_{e\mu}$ . We emphasize that at baselines of  $> 7000$  Km, matter effects in  $P_{\mu\tau}$  are important under certain conditions and can be large. The muon survival rates in experiments with very long baselines thus depend on matter effects in both  $P_{\mu\tau}$  and  $P_{e\mu}$ . We also indicate where these effects provide sensitivity to  $\theta_{13}$ , and identify ranges of energies and baselines where the event rates increase with decreasing  $\theta_{13}$ , providing a useful handle to probe small values of this parameter. The effect of parameter degeneracies in the three probabilities at these baselines and energies is studied in detail and large parts of the parameter space are identified which are free from these degeneracies. In the second part of the paper, we focus on using the matter effects studied in the first part as a means of determining the mass hierarchy via atmospheric neutrinos. Realistic event rate calculations are performed for a charge discriminating 100 kT iron calorimeter which demonstrate the possibility of realising this very important goal in neutrino physics. It is shown that for atmospheric neutrinos, a careful selection of energy and baseline ranges is necessary in order to obtain a statistically significant signal, and that the effects are largest in bins where matter effects in both  $P_{e\mu}$  and  $P_{\mu\tau}$  combine constructively. Under these conditions, upto a 4 $\sigma$  signal for matter effects is possible (for  $\theta_{31} > 0$ ) within a timescale appreciably shorter than the one anticipated for neutrino factories.

**Keywords:** Atmospheric neutrinos, Long baselines, Neutrino Oscillations, Matter effects.

---

E-mail: raj@riemmet.in

<sup>y</sup>E-mail: pomita@riemmet.in

<sup>z</sup>E-mail: sruba@riemmet.in

<sup>x</sup>E-mail: mpoonam@riemmet.in

<sup>t</sup>E-mail: uma@phy.iitb.ac.in

---

## Contents

1. Introduction	1
2. Discussion of the Matter Probabilities : $P_e^m$ , $P^m$ , and $P^m$	5
2.1 Review of $P_e$ in matter	5
2.2 Matter effects in P	7
2.3 Matter effects in P	13
2.4 Degeneracies in the determination of oscillation parameters at very long baselines	16
3. Determining the Mass Hierarchy via Atmospheric in a charge discriminating Detector	22
4. Conclusions	31

---

## 1. Introduction

It is fair to say that over the last few years there has been a qualitative shift in the nature of the goals to be pursued in neutrino physics. This has been the result of steadily accumulating evidence in favour of non-zero neutrino mass and flavour oscillations. Results from atmospheric neutrino experiments [17], corroborated by the accelerator beam based K2K experiment [8] have provided firm evidence for  $\nu_\mu \rightarrow \nu_\tau$  oscillations with maximal (or almost maximal) mixing. The solar neutrino results [9,16], when combined with the results of the reactor based KamLAND experiment [17], have established the LMA-MSW solution [18] as the most favoured explanation for the solar neutrino deficit. For recent global analyses of solar, reactor, accelerator and atmospheric data, see [19,22]. In Table 1, we summarize the best-fit values and  $3\sigma$  intervals of allowed values of important oscillation parameters gleaned from experiments so far obtained from global three flavour neutrino analysis [19,21].

The shift has been from a search for understanding the particle physics and/or the astrophysics driving the solar and atmospheric neutrino deficits to one where we seek to make increasingly precise measurements of neutrino mass and mixing matrix parameters. Experiments planned to yield results over the next ten to fifteen years thus reflect this change of emphasis. A significant number of the planned

Parameter	best-fit	3 $\sigma$
$\theta_{21}$ [ $10^{-5} \text{eV}^2$ ]	8.3	7.2 { 9.1
$\theta_{31}$ [ $10^{-3} \text{eV}^2$ ]	2.2	1.4 { 3.3
$\sin^2 \theta_{12}$	0.30	0.23 { 0.38
$\sin^2 \theta_{23}$	0.50	0.34 { 0.68
$\sin^2 \theta_{13}$	0.00	0.047

Table 1: Best-fit values and  $3\sigma$  intervals for three flavour neutrino oscillation parameters from global data including solar, atmospheric, reactor (KamLAND and CHOOZ) and accelerator (K2K) experiments [19,21].

projects are long baseline<sup>1</sup> endeavours using either (a) a conventional proton beam colliding with a target to produce pions which then decay to give muon neutrinos, or (b) super-beams, which are essentially technologically upgraded versions of present conventional beams, or, finally, (c) reactor sources with both near and far detectors for reduced systematic errors.

To begin with, we enumerate and briefly describe the planned projects in the three categories above which are expected to give results over the next decade or decade and a half. For a recent detailed study of their capabilities we refer the reader to [23] and references therein.

Conventional beam experiments will have as their primary goal the improvement in the precision of the atmospheric oscillation parameters,  $\theta_{31}$  and  $\sin^2 2\theta_{23}$ . MINOS [24], located in the US, with a baseline from Fermilab to Soudan, MN (735 Km), will utilize a 5.4 kT magnetized iron calorimeter and initially an  $\langle E \rangle \sim 3 \text{ GeV}$  to primarily measure muon survival events. By measuring the absolute event rate and the energy distribution for muons produced via charged current (CC) scattering,  $\theta_{31}$  may be determined to within about 10-20% of the current best-fit value. In addition, by measurements in the electron appearance channel, MINOS may provide a possibly improved upper bound on  $\sin^2 2\theta_{13}$ , by a factor of 1.5 to 2. In Europe, the two experiments planned in this category are ICARUS [25], a 2.35 kT liquid Argon detector, and OPERA [26] a 1.65 kT emulsion cloud chamber, which will ride the 732 Km CERN to Gran

<sup>1</sup>By "long baseline" we actually mean the L/E range of about 50-500 Km/GeV. For accelerator experiments, this translates to baselines conventionally termed "long", but for the lower reactor neutrino energies, the baselines are actually 1-2 Km.

Sasso baseline and will be powered by the CNGS beam. The beam energy is higher, resulting in neutrinos which are kinematically capable of producing leptons ( $E > 17 \text{ GeV}$ ). In addition, these detectors can identify muons and electrons. It is thus anticipated that in addition to an improved precision in  $\theta_{31}$ , an improvement in the current bound on  $\sin^2 2\theta_{13}$  may be possible at the same levels as anticipated with MINOS.

Superbeam experiments utilise the same basic principle used in conventional beam experiments, but incorporate substantial technological improvements. This includes higher power beams and the idea of an "off-axis" location for the detector. One of the planned projects is the 295 Km Japanese J-PARC project [27], with Super-K (22.5 kT) as the detector and  $E > 0.76 \text{ GeV}$ . Similarly, NuMI [28] is planned for location in the US, with a 712 Km (or possibly somewhat higher) baseline terminating in a 50 kT calorimeter and  $E > 2.2 \text{ GeV}$ . Both experiments primarily aim at heightened sensitivity to  $\sin^2 2\theta_{13}$  via the electron appearance channel. It is anticipated that the upper bound on this parameter will be improved by a factor of four over a five year running period.

As discussed in [23], the combination of conventional and superbeam experiments over the next 10-12 years will improve the precision on  $\theta_{31}$  by an order of magnitude, while the improvement in  $\sin^2 2\theta_{23}$  will be much more modest, i.e. by a factor of about two.

Planned experiments in the reactor category include KASKA in Japan [29], several in the US [30,31] and an upgraded version of CHOOZ [32,33], called Double-CHOOZ [34]. Reactor experiments detect the electron anti-neutrino flux by the inverse beta-decay process, and focus on improved measurements of  $\sin^2 2\theta_{13}$ , using a near detector to lower systematics. A factor of six improvement in the present upper bound on this parameter is expected.

To summarize, the above experiments will, over the next 10-15 years, greatly improve the precision on  $\theta_{31}$ , effect a very modest improvement in the existing measurements for  $\sin^2 2\theta_{23}$ , and improve the upper bound on  $\sin^2 2\theta_{13}$  by a factor of two to six, depending on the experiment. We note that given their insensitivity to matter effects,<sup>2</sup> they will not be able to conclusively determine the sign of  $\theta_{31}$  and thus will not establish whether neutrino masses follow a normal hierarchy or an inverted one. This may thus leave one of the major questions of neutrino physics unresolved over the timescale considered here (10-15 years). Besides requiring a baseline long enough to allow matter oscillations to develop, the resolution of this issue, in general, requires a detector which can distinguish the sign of the lepton

---

<sup>2</sup>All baselines for the listed experiments are below 800 Km.

produced in a CC interaction. Over a longer term, progress in this direction may be possible via the proposed mega-ton Water Cherenkov detectors. Even though they do not have the capability to distinguish the charge on an event by event basis, once enough statistics are collected ( $\sim 2$  Mega-ton yr exposures), it may be possible to use the differences in total and differential CC cross-sections between neutrinos and anti-neutrinos to obtain a statistical determination of the sign of  $\theta_{31}$  [35,36]. Additionally, if neutrino factories are built, they will be able to resolve this question in a definitive fashion [37]. This paper examines the possibility of resolving this issue using atmospheric muon neutrinos over the same (shorter) time-frame as the long baseline program described above.

In the first part of this paper, we study the physics related to the sensitivity of the muon neutrino survival probability to matter. In general,  $P_{\mu\mu} = 1 - P_{e\mu} - P_{\mu\tau}$ , and one normally assumes that the dependence of  $P_{\mu\mu}$  on matter effects arises primarily from its  $P_{e\mu}$  component while matter effects in  $P_{\mu\tau}$  remain small. This is because  $\nu_e$  and  $\nu_\mu$  have the same coherent interactions with the Earth's matter. In [38] recently, it was shown that contrary to expectations, the  $\nu_e \rightarrow \nu_\mu$  oscillation probability  $P_{e\mu}$  can also undergo significant change (for instance, a reduction as high as 70% or an increase of 15%) at very long baselines ( $> 6000$  Km) over a broad band of atmospheric (GeV) neutrino energies due to matter effects. Given the fact that the atmospheric neutrino flux is a sharply falling function of energy in the few GeV range ( $\frac{dN}{dE} \propto E^{-3.6}$ ) and that the production of leptons via CC is kinematically suppressed here, a direct observation of this effect via appearance in an atmospheric neutrino experiment may be difficult. However, large matter effects in  $P_{e\mu}$  certainly cause correspondingly large changes in  $P_{\mu\mu}$ , and we explore the consequences of this in our paper. In particular, in the next section, we systematically discuss the interrelation between the three probabilities  $P_{e\mu}$ ,  $P_{\mu\tau}$  and  $P_{\mu\mu}$  and study the ranges of energies and pathlengths where they combine in a synergistic manner to give large effects. We also examine the problem of parameter degeneracies in these oscillation probabilities with reference to very long baselines.

The remaining part of the paper studies observational consequences of these effects for muon survival rates with particular emphasis on resolving the hierarchy issue in an atmospheric neutrino setting, using a detector capable of lepton charge discrimination. Earlier studies of this were undertaken in [39,40] and, more recently, in [41-43]. We also note that the muon survival rate is a major constituent of the signal in SuperKamioke (SK) [2,3], the planned BNL-Homestake [44] large water Cherenkov detector, the Fermilab to Kamioke [45] project, and several detectors considered for future long baseline facilities, for which the discussion below may be of relevance.

## 2. Discussion of the Matter Probabilities : $P_e^m$ , $P^m$ , and $P^m$

Analytical expressions for oscillation probabilities in vacuum and matter of constant density have been extensively studied in the literature [46-57]. The neutrino flavour states are linear superpositions of the mass eigenstates with well-defined masses :

$$|j\rangle = \sum_i U_{ij} |i\rangle; \quad (2.1)$$

where  $U$  is a  $3 \times 3$  unitary matrix known as the Pontecorvo-Maki-Nakagawa-Sakata mixing matrix. We use the standard parametrization of  $U$  in terms of three mixing angles and a Dirac-type phase (ignoring Majorana phases), viz.

$$U = \begin{pmatrix} c_{12}c_{13} & s_{12}c_{13} & s_{13}e^{-i\phi_{CP}} \\ c_{23}s_{12} & s_{23}s_{13}c_{12}e^{i\phi_{CP}} & s_{23}c_{13} \\ s_{23}s_{12} & c_{23}s_{13}c_{12}e^{i\phi_{CP}} & c_{23}c_{13} \end{pmatrix} A; \quad (2.2)$$

where  $c_{ij} = \cos \theta_{ij}$ ,  $s_{ij} = \sin \theta_{ij}$  and  $\phi_{CP}$  is the CP-violating phase.

For the purpose of our discussion in the first three subsections here, besides the approximation of constant density, we set  $\theta_{21} = \theta_{31} = 0$ . Consequently the mixing angle  $\theta_{12}$  and the CP phase  $\phi_{CP}$  drop out of the oscillation probabilities. This approximation simplifies the analytical expressions and facilitates the qualitative discussion of matter effects. We have checked that this works well (upto a few percent) at the energies and length scales relevant here. However, all the plots we give in this paper are obtained by numerically solving the full three flavour neutrino propagation equation assuming the PREM [58] density profile for the earth. We use  $\theta_{31} = 0.002 \text{ eV}^2$  and  $\sin^2 2\theta_{23} = 1$  unless otherwise mentioned. Further, the numerical calculations assume  $\theta_{21} = 8.3 \times 10^{-5} \text{ eV}^2$ ,  $\sin^2 \theta_{12} = 0.27$  [17] and  $\phi_{CP} = 0$ . The effect of varying the CP phase over the entire range (0 to  $2\pi$ ) will be taken up in Subsection 2.4, where we include analytic expressions which take into account all sub-leading effects and discuss the associated parameter degeneracies.

### 2.1 Review of $P_e$ in matter

We first review  $\nu_e$  oscillations in matter [59,60]. In vacuum, the  $\nu_e$  oscillation probability is

$$P_e^v = \sin^2 \theta_{23} \sin^2 2\theta_{13} \sin^2 (1.27 \theta_{31} L = E); \quad (2.3)$$

where  $\theta_{31} = \frac{m_3^2 - m_1^2}{2E}$  is expressed in  $\text{eV}^2$ ,  $L$  in Km and  $E$  in GeV. In the constant density approximation, matter effects can be taken into account by replacing  $\theta_{31}$  and  $\theta_{13}$  in Eq. 2.3 by their matter dependent values, i.e.,

$$P_e^m = \sin^2 \theta_{23} \sin^2 2\theta_{13}^m \sin^2 (1.27 \theta_{31}^m L = E); \quad (2.4)$$

Here  $\theta_{31}^m$  and  $\sin^2 \theta_{13}^m$  are given by<sup>3</sup>

$$\theta_{31}^m = \arctan \frac{p}{(\theta_{31} \cos 2\theta_{13} - A)^2 + (\theta_{31} \sin 2\theta_{13})^2}$$

$$\sin^2 \theta_{13}^m = \sin^2 \theta_{13} \frac{\theta_{31}^m}{\theta_{31}} \quad (2.5)$$

where

$$A = \frac{p}{2} \frac{1}{G_F n_e E} = 0.76 \cdot 10^{-4} (\text{gm/cc}) E (\text{GeV})$$

The resonance condition is  $A = \theta_{31} \cos 2\theta_{13}$ , which gives

$$E_{\text{res}} = \frac{\theta_{31} \cos 2\theta_{13}}{2 \frac{p}{2} G_F n_e} \quad (2.6)$$

Naively, one would expect  $P_e^m$  to be maximum at  $E = E_{\text{res}}$  since  $\sin^2 \theta_{13}^m = 1$ . But this is not true in general because at this energy  $\theta_{31}^m$  takes its minimum value of  $\theta_{31} \sin 2\theta_{13}$  and  $P_e^m$  remains small for pathlengths of  $L \sim 1000$  Km. If  $L$  is chosen suitably large so as to satisfy  $(1.27 \theta_{31} \sin 2\theta_{13} L = E) = 4$ , then  $P_e^m$  can attain values  $0.25$  for  $\sin^2 2\theta_{13} = 1$ . For  $\theta_{31} = 0.002 \text{ eV}^2$  and  $\sin^2 2\theta_{13} = 0.1$ , one needs  $L \sim 6000$  Km to satisfy the above condition.

In particular,  $P_e^m$  is maximum when both

$$\sin^2 \theta_{13}^m = 1$$

and

$$\sin^2 (1.27 \theta_{31} L = E) = 1 \text{ or; } (1.27 \theta_{31} L = E) = [(2p + 1) \pi]$$

are satisfied. This occurs when  $E_{\text{res}} = E_{\text{peak}}^m$ . This gives the condition [38,39]:

$$L_e^{\text{max}}, \frac{(2p + 1) 5.18 \cdot 10^3}{\tan 2\theta_{13}} \text{ Km gm/cc:} \quad (2.7)$$

Here,  $p$  takes integer values. This condition is independent of  $\theta_{31}$  but depends sensitively on  $\theta_{13}$ . In Figure 1, we plot  $L_e^{\text{max}}$  vs  $L$  for the earth (calculated using the PREM profile), where  $\rho_{\text{av}}$  is the average density for a given baseline  $L$ . We identify the particular values of  $L_e^{\text{max}}$  which satisfy Eq. 2.7 with  $p=0$  for three different values of  $\sin^2 2\theta_{13}$ . These occur at  $L \sim 10200$  Km,  $7600$  Km and  $11200$  Km for  $\sin^2 2\theta_{13} = 0.1; 0.2$  and  $0.05$  respectively. This identifies the baselines at which  $P_e^m$  is maximized. Additionally, the relatively wide spacing between them demonstrates the sensitivity to  $\theta_{13}$ . At and around the resonant energies and these baselines (depending on the value of  $\theta_{13}$ )  $P_e^m$  significantly impacts not only  $P_e$ , but also  $P_\mu$ , as we discuss below. Note that for higher values of  $p$ , the baselines for maximum matter effect are greater than the Earth's diameter. Hence  $p=0$  is the only relevant value of  $p$  in this case.

<sup>3</sup>Here and subsequently we use  $\theta_{31} > 0$  which corresponds to matter effects for neutrinos. For anti-neutrinos,  $A \rightarrow -A$  and we need  $\theta_{31} < 0$  for significant matter effects.

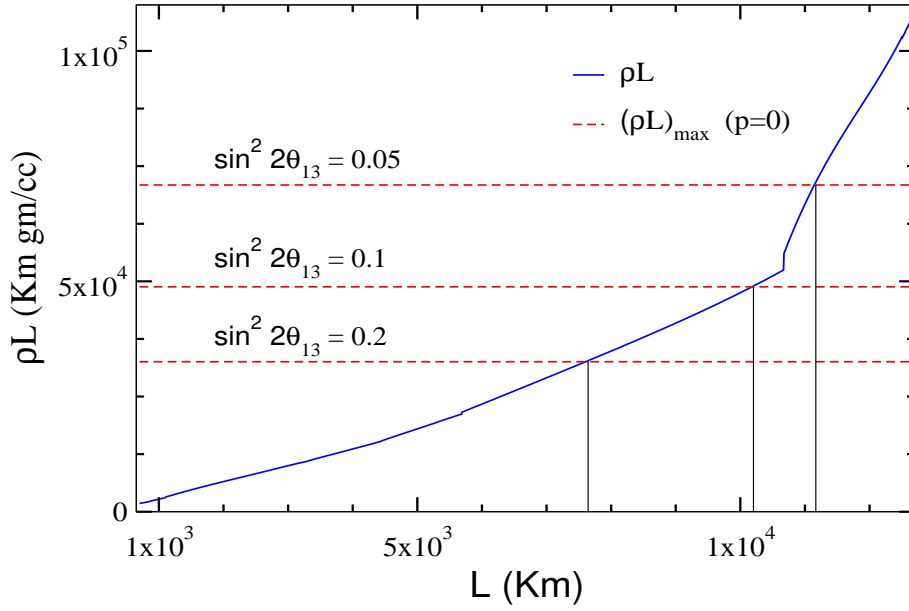


Figure 1:  $\rho L$  plotted vs  $L$ . Horizontal lines correspond to  $L_e^{\max}$  for different values of  $\theta_{13}$ .

## 2.2 Matter effects in P

In vacuum we have

$$\begin{aligned}
 P^v &= \cos^4 \theta_{13} \sin^2 2\theta_{23} \sin^2 (\Delta 27_{31} L = E); \\
 &= \cos^2 \theta_{13} \sin^2 2\theta_{23} \sin^2 (\Delta 27_{31} L = E) \\
 &\quad \cos^2 2\theta_{23} P_e^v
 \end{aligned} \tag{2.8}$$

Including the matter effects changes this to [57,60]

$$\begin{aligned}
 P^m &= \cos^2 \theta_{13}^m \sin^2 2\theta_{23} \sin^2 [\Delta 27_{31} (1 + A + \frac{m}{31}) L = 2E] \\
 &+ \sin^2 \theta_{13}^m \sin^2 2\theta_{23} \sin^2 [\Delta 27_{31} (1 + A - \frac{m}{31}) L = 2E] \\
 &\quad \cos^2 2\theta_{23} P_e^m
 \end{aligned} \tag{2.9}$$

Compared to  $P_e^m$ , these expressions have a more complex matter dependence. This occurs due to the more complicated change of  $\theta_{13}$  and  $\theta_{23}$  in the flavour content of the matter dependent mass eigenstates. Labeling the vacuum mass eigenstates as  $\nu_1$ ,  $\nu_2$  and  $\nu_3$ , in the approximation where  $\theta_{21} = 0$ ,  $\nu_1$  is almost entirely  $\nu_e$  and  $\nu_2$  has no  $\nu_e$  component<sup>4</sup>. Inclusion of the matter term  $A$  leaves  $\nu_2$  untouched but gives a non-zero matter dependent mass to  $\nu_1$ . As the energy increases, the  $\nu_e$  component

<sup>4</sup>While  $\theta_{12}$  is undetermined in the approximation  $\theta_{21} = 0$ , it also drops out of the mixing matrix in this approximation, and the weights of  $\nu_e$  in  $\nu_1$  and  $\nu_2$  do not depend on it.

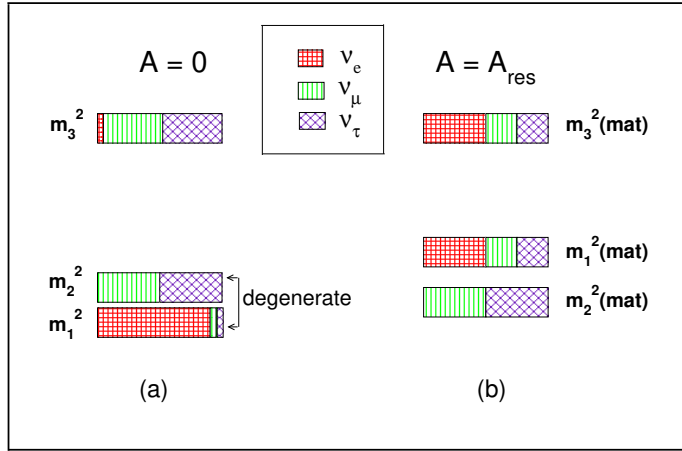


Figure 2: The flavor composition of mass eigenstates in vacuum ( $A = 0$ ) and in matter at resonance ( $A = A_{res}$ ). The vacuum parameters used are  $\sin^2 2_{23} = 1.0$  and  $\sin^2 2_{13} = 0.1$ .

of  $m_1^m$  decreases and the  $\nu_e$  components increase such that at resonance energy they are 50%. Similarly, increasing energy increases the  $\nu_e$  component of  $m_3^m$  (and reduces the  $\nu_\tau$  components) so that at resonance it becomes 50%. Thus in the resonance region, all three matter dependent mass-eigenstates  $m_1^m$ ;  $m_2^m$  and  $m_3^m$  contain significant  $\nu_e$  and  $\nu_\mu$  components. Hence, the matter dependent  $\nu_e \rightarrow \nu_\mu$  oscillation probability will depend on all three matter modified mass-squared differences. In Figure 2 we show the flavor composition of the three mass states in vacuum and at resonance.

We are interested in finding ranges of energy and pathlengths for which there are large matter effects in  $P^m$ , i.e., for which  $P^m = P^m - P^v$  is large. To this end, it is useful to examine the set of probability plots given in Figure 3. The plots display the variation of  $P^m$  with neutrino energy  $E$  for baselines of 8000 Km, 9700 Km and 10500 Km respectively, with each of the terms in Eq. 2.9 plotted separately.  $P^m(1)$ ,  $P^m(2)$  and  $P^m(3)$  in the figure refer to the first, second and third term in Eq. 2.9 respectively, with the third term plotted incorporating its negative sign.

Additionally, the plots display the full vacuum probability,  $P^v$ . The approximate average density at these baselines is  $\rho_{av} \approx 4.5$  gm/cc, hence one gets  $E_{res} \approx 5$  GeV from Eq. 2.6. The vacuum peaks, of course, shift with baseline and we see that a significantly broad peak gradually positions itself above the resonant energy at the baselines shown in the figure. We use this fact in (i) below.

We show that appreciable changes in  $P^m$  occur for two different sets of conditions, leading in one case to a sharp decrease from a vacuum maximum and in another to a smaller but extended increase over a broad range of energies. Both are discussed below in turn.

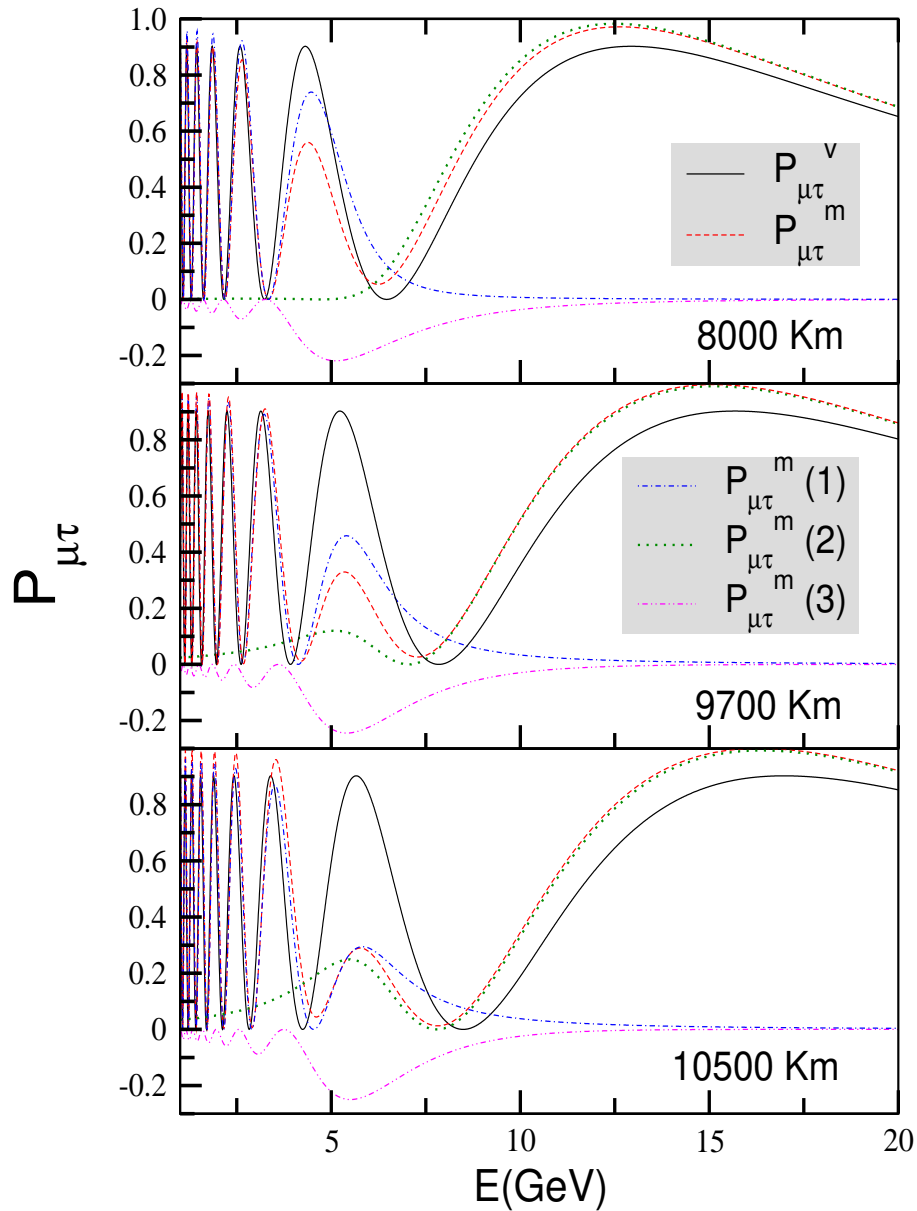


Figure 3: The variation of  $P_{\mu\tau}$  in matter,  $P_{\mu\tau}^m$  and in vacuum,  $P_{\mu\tau}^v$  with neutrino energy  $E$  for three different baselines of 8000 Km, 9700 Km and 10500 Km respectively. Each of the terms in Eq. 2.9 are also shown in the three plots:  $P_{\mu\tau}^m(1)$  is term 1,  $P_{\mu\tau}^m(2)$  is term 2 and  $P_{\mu\tau}^m(3)$  is term 3 respectively.

(i) Large decrease in  $P_{\mu\tau}^m$  in the resonance region :

As is evident in Figure 3, at energies appreciably below resonance, term 1 in Eq. 2.9 (i.e. the one with  $\cos^2 \theta_{13}^m$ ) is very nearly equal to  $P_{\mu\tau}^v$ . This is because  $\theta_{13}^m = \theta_{13}$ ,  $A \ll \Delta m_{31}^2$ ;  $\theta_{31}^m \approx \theta_{31}$ . Term 2, the  $\sin^2 \theta_{13}^m$  term, is nearly zero. Similarly, term 3 is also very small. As we increase the energy and approach resonance,  $\cos^2 \theta_{13}^m$  begins to decrease sharply, deviating from its vacuum values,

while  $\sin^2 \theta_{13}^m$  increases rapidly. However, if resonance is in the vicinity of a vacuum peak, which is the case at and around the baselines shown in Figure 3, then the decrease in the  $\cos^2 \theta_{13}^m$  term has a much stronger impact on  $P^m$  than the increase in the  $\sin^2 \theta_{13}^m$  term, since the latter starts out at zero while the former is initially close to its peak value (1). As a result,  $P^m$  falls sharply. This fall is enhanced by the third term in Eq. 2.9, which is essentially  $0.5 P_e^m$  (which is large due to resonance), leading to a large overall drop in  $P^m$  from its vacuum value. Note that the requirement that we be at a vacuum peak to begin with forces  $P$  to be large and negative, with the contributions from the first and the third term reinforcing each other.

The criterion for a maximum matter effect,  $E_{res} = E_{peak}^v$ , leads to the following condition:

$$L^{max} = (2p + 1) \frac{5.18 \times 10^3 (\cos 2\theta_{13}) K m}{g m} = cc \quad (2.10)$$

Unlike Eq. 2.7, which has a  $\tan 2\theta_{13}$  in its denominator, Eq. 2.10 has a much weaker dependence on  $\theta_{13}$ .

From Eq. 2.8 and Eq. 2.9, we write

$$\begin{aligned} P &= P^m - P^v \\ &= \sin^2 2\theta_{23} [ \cos^4 \theta_{13} \sin^2 (1.27 \theta_{31} L = E) \\ &+ \cos^2 \theta_{13} \sin^2 [1.27 (\theta_{31} + A + \theta_{31}^m) L = 2E] \\ &+ \sin^2 \theta_{13} \sin^2 [1.27 (\theta_{31} + A + \theta_{31}^m) L = 2E] \\ &\quad \sin^2 \theta_{13} \cos^2 \theta_{13} \sin^2 (1.27 \theta_{31} L = E) ] \end{aligned} \quad (2.11)$$

Incorporating the  $E_{res} = E_{peak}^v$  condition (Eq. 2.10) leads to

$$P = \frac{h}{i} \cos^4 \theta_{13} \sin^2 2\theta_{13} (2p + 1) \frac{1}{4} \quad (2.12)$$

We note that, in general,  $P$  (at  $E_{res} = E_{peak}^v$ ) will be larger for higher values of both  $p$  and  $\theta_{13}$ . For  $p=1$  and  $\sin^2 2\theta_{13} = 0.1$ ,  $E_{res} = E_{peak}^v$  occurs at 9700 Km (from Eq. 2.10) and  $P = 0.7$  (from Eq. 2.12). For  $p=0$ , Eq. 2.10 gives  $L^{max} = 4400$  Km for  $\sin^2 2\theta_{13} = 0.1$ . However,  $P$  is roughly one-tenth of the  $p=1$  case. In general, for a given baseline, the choice of an optimal  $p$  is also dictated by the constraint that the vacuum peak near resonance have a breadth which makes the effect observationally viable. Note that for  $\sin^2 2\theta_{13} = 0.05$  and  $0.2$ , Eq. 2.10 gives the distances of maximum matter effect as 9900 and 9300 Km for  $p=1$ . Because of the weaker dependence on  $\theta_{13}$  here compared to  $P_e^m$  (Eq. 2.7), the distances for various values of  $\theta_{13}$  are bunched together in the vicinity of 9500 Km.

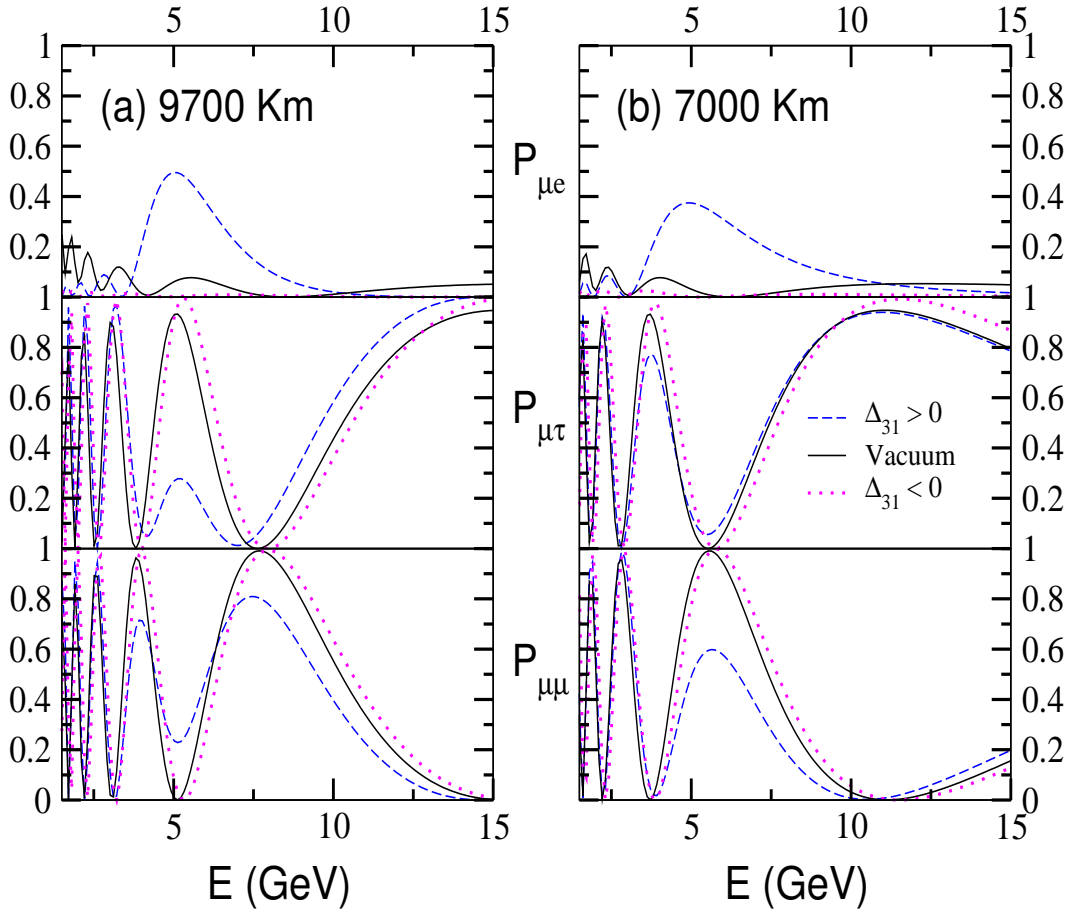


Figure 4:  $P_{\mu e}$  and  $P_{\mu\tau}$  plotted as a function of neutrino energy,  $E$  (in GeV) in presence of matter and in vacuum for both signs of  $m_{31}^2$  for two different baseline lengths, (a) for  $L = 9700$  Km and (b) for  $L = 7000$  Km. These plots use  $\Delta_{31} = 0.002 \text{ eV}^2$  and  $\sin^2 2_{13} = 0.1$ .

In Figure 4 (a) we show all three matter and vacuum probabilities for 9700 Km. In these plots  $\Delta_{31}$  is taken as  $0.002 \text{ eV}^2$  which gives  $E_{\text{res}} = E_{\text{peak}}^v \approx 5 \text{ GeV}$ . The middle panel of Figure 4 (a) shows that near this energy  $P_{\mu\tau}^m$  ( $\approx 0.33$ ) is appreciably lower compared to  $P_{\mu\tau}^v$  ( $\approx 1$ ). Thus the drop due to matter effect is 0.67, which agrees well with that obtained in the paragraph above using the approximate expression Eq. 2.12.

In Figure 5 we show the  $\Delta_{13}$  sensitivity of  $P_{\mu e}^m$  at 9700 Km<sup>5</sup>. In particular, at  $E_{\text{res}} \approx E_{\text{peak}}^v$  the strong dependence on  $\Delta_{13}$  is also governed by Eq. 2.12 above. Unlike  $P_{\mu e}^m$ , where the event-rate decreases as  $\Delta_{13}^2$  for small values of  $\Delta_{13}$ , the appearance rate at  $E_{\text{res}} = E_{\text{peak}}^v$  increases with decreasing  $\Delta_{13}$ . As  $\sin^2 2_{13}$  goes from 0.2 to 0,  $P_{\mu e}^m$  varies from 0.05 to 1. For very small values of  $\sin^2 2_{13}$  ( $< 0.05$ ) it will be impossible to see a maximal resonance enhancement

<sup>5</sup> $P_{\mu e}^m$  develops good sensitivity to  $\Delta_{13}$  only at around  $L = 9700$  Km. Even at  $L = 7000$  Km, its sensitivity to matter effects is very poor (Figure 4 (b), middle panel).

in  $P_e$  because the distance for which this occurs exceeds the diameter of the earth. However, the observation of a maximal resonant suppression in  $P$  is possible, even for very small values of  $\theta_{13}$  [38]. This possibility, of course, is subject to the kinematic suppression of the tau production cross-section at the energies under consideration here, which may necessitate a high luminosity source, such as a neutrino factory, to observe these effects in a tau appearance experiment. However, the features in  $P^m$  discussed here can translate into observable effects for muon survival measurements in an atmospheric neutrino experiment, and this is the aspect we have focussed on in Section 3.

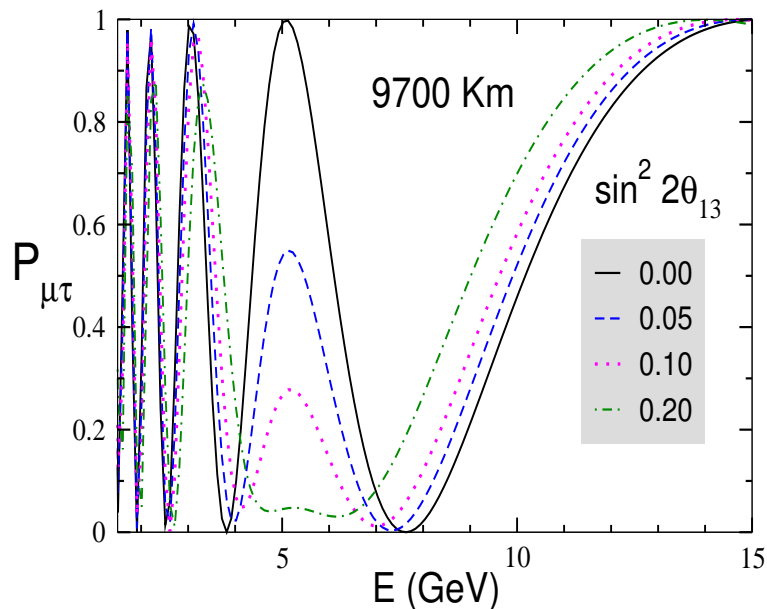


Figure 5: The plot shows sensitivity to  $\theta_{13}$  in case of  $P_{\mu\tau}$  for a baseline length of 9700 Km. The value of  $\theta_{31}$  is taken to be  $0.002 \text{ eV}^2$ .

(ii) Increase in  $P^m$  away from resonance :

We now discuss the second scenario for which  $P^m$  can differ appreciably from  $P^v$ . This happens away from resonance, and is evident in Figure 4 (a) (central panel) in the energy range 7.5 GeV – 15 GeV. This effect is an enhancement rather than a drop, i.e.,  $P$  is now positive, unlike the previous case.

$P_e$  is small in most of the latter part of the energy region under consideration and does not contribute in an important way overall (Figure 4 (a) (top panel)). The dominant contribution to this enhancement arises from the  $\sin^2 \theta_{13}^m$  term

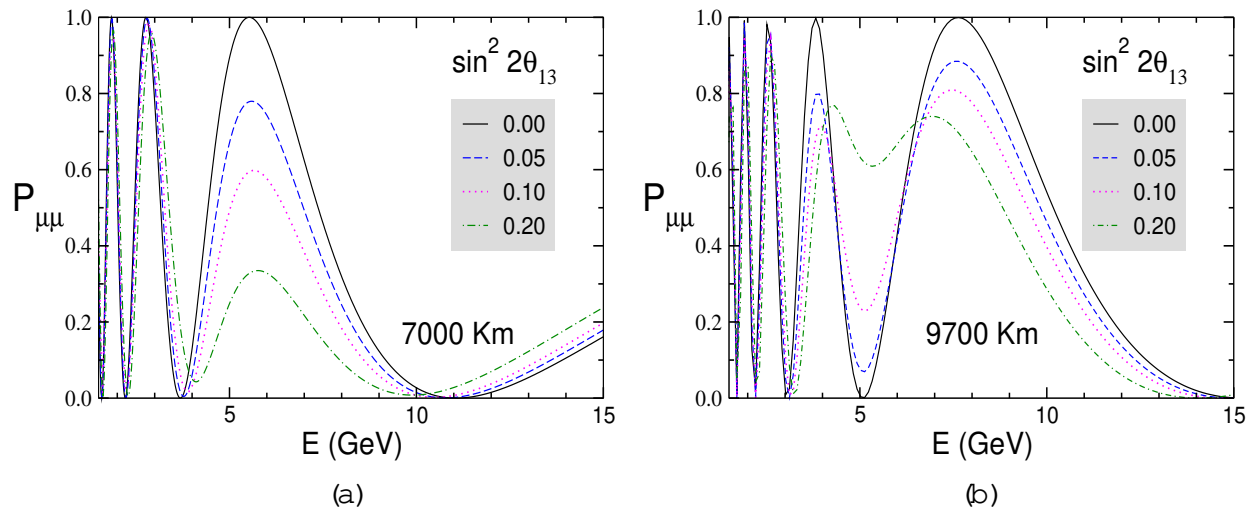


Figure 6: Figure (a) and (b) depict  $P_{\mu\mu}$  in matter plotted against the neutrino energy,  $E$  (in GeV) for different values of  $\theta_{13}$  and two baseline lengths, viz, 7000 Km and 9700 Km, respectively.

in  $P^m$  (Eq. 2.9) which is large for  $E \gg E_{res}$ . Since  $(\theta_{31} + A \frac{m_{31}}{2})^2 \approx \theta_{31}^2$  for these energies, we obtain an enhancement (15%) which follows the vacuum curve. The difference between the two curves, vacuum and matter, largely reflects the difference between the  $\cos^4 \theta_{13}$  multiplicative term in the vacuum expression Eq. 2.8 and the  $\sin^2 \theta_{13}$  multiplicative term in Eq. 2.9. While this effect is smaller compared to the effect discussed in (i) above, it occurs over a broad energy band and can manifest itself in energy integrated event rates.

### 2.3 Matter effects in $P$

In vacuum  $P$  is given by

$$\begin{aligned}
 P^v &= 1 - P^v_e \\
 &= 1 - \cos^4 \theta_{13} \sin^2 2\theta_{23} \sin^2 (1.27 \theta_{31} L = E) \\
 &\quad - \sin^2 2\theta_{23} \sin^2 \theta_{13} \sin^2 (1.27 \theta_{31} L = E)
 \end{aligned} \tag{2.13}$$

Including the matter effects changes this to

$$\begin{aligned}
 P^m &= 1 - P^m_e \\
 &= 1 - \cos^2 \theta_{13} \sin^2 2\theta_{23} \sin^2 [1.27 (\theta_{31} + A \frac{m_{31}}{2}) L = 2E] \\
 &\quad - \sin^2 \theta_{13} \sin^2 2\theta_{23} \sin^2 [1.27 (\theta_{31} + A \frac{m_{31}}{2}) L = 2E] \\
 &\quad - \sin^4 2\theta_{23} \sin^2 \theta_{13} \sin^2 (1.27 \frac{m_{31}}{2} L = E)
 \end{aligned} \tag{2.14}$$

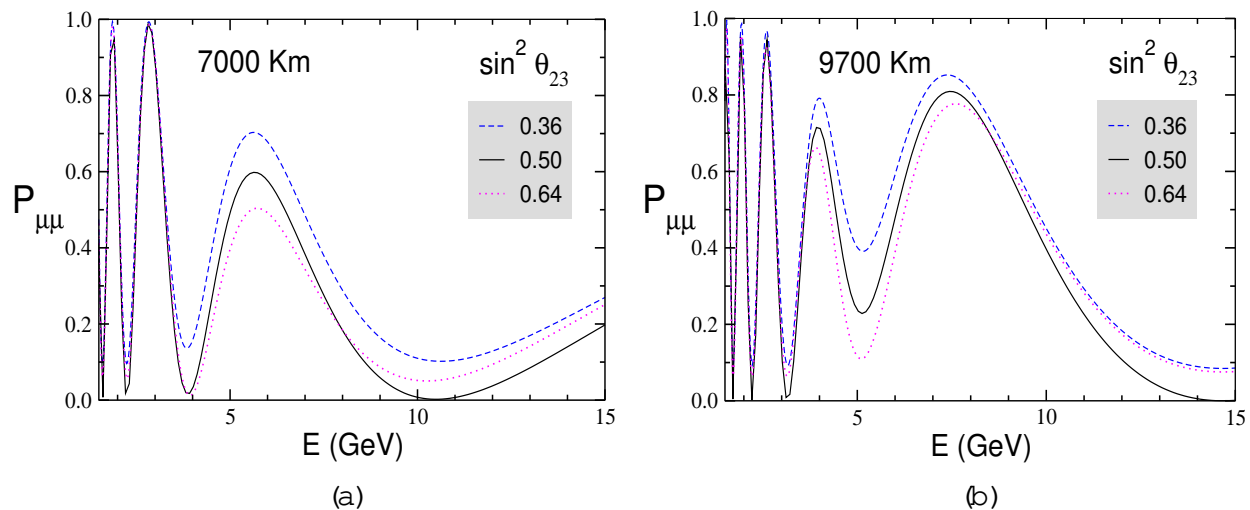


Figure 7: Figure (a) and (b) depict  $P_{\mu\mu}$  in matter plotted vs  $E$  (in GeV) for different values of  $\theta_{23}$  and two baseline lengths, viz, 7000 Km and 9700 Km respectively, for  $\sin^2 2\theta_{13} = 0.1$ . The value of  $\Delta m_{31}^2$  is taken to be  $0.002 \text{ eV}^2$ .

The deviation of  $P_{\mu\mu}^m$  from  $P_{\mu\mu}^v$  clearly results from the combined effects in  $P_{\mu\mu}^m$  and  $P_{ee}^m$ . In order to quantify the extent of deviation, we define,

$$P_{\mu\mu}^m = P_{\mu\mu}^v + P_{ee}^m \quad (2.15)$$

Below we illustrate the various conditions which can give rise to a significant change in  $P_{\mu\mu}$  due to matter effects arising in both  $P_{\mu\mu}$  and  $P_{ee}$ :

(a) Large, negative  $P_{\mu\mu}$  and positive  $P_{ee}$

Large and negative  $P_{\mu\mu}$  corresponds to the case (i) discussed in Subsection 2.2. In this case,  $P_{ee}$  is positive, so the signs of the two changes are opposite and hence the two terms (Eq. 2.15) do not contribute in consonance. However, the resulting increase in  $P_{\mu\mu}$  is still significant (20%), given the magnitude of the change (70%) in  $P_{\mu\mu}$ . This is visible in the bottom panel of Figure 4 (a), in the energy range 4-6 GeV.

(b) Positive  $P_{\mu\mu}$  and small  $P_{ee}$

This case corresponds to a significant drop in  $P_{\mu\mu}^m$ , which is seen in Figure 4 (a) (bottom panel) in the energy range 7-15 GeV. The enhancement in  $P_{\mu\mu}^m$  (corresponding to the case (ii) discussed in Subsection 2.2) is reflected in the decrease in  $P_{\mu\mu}^m$  compared to its vacuum value.

(c) Small  $P_{\mu\mu}$  and large, positive  $P_{ee}$

This situation occurs when a minimum in the vacuum value of  $P_{\mu\mu}$  resides in the proximity of a resonance. The condition for a minimum in  $P_{\mu\mu}$  is

1.27  $P_{31}^m = E = p$ . In this region, the rapidly changing  $\sin^2 \frac{m}{13}$  and  $\cos^2 \frac{m}{13}$  increase  $P$  from its vacuum value of 0 to about 0.1. At the same time,  $P_e$  undergoes an increase of 0.3, thus leading to a net change of  $P = 0.4$  (the three panels of Figure 4 (b)). Note that the above condition corresponds to a vacuum peak of  $P$  and the 40% drop of its value makes this energy range (4-10 GeV) suitable for searching for matter effects. Substituting  $E$  as  $E_{res}$  gives the distance for maximum matter effect in  $P$  as

$$L^{max} = p \cdot 10^4 (\cos 2_{13}) \text{ Km} \quad (2.16)$$

For  $p=1$  this turns out to be 7000 Km. This effect [59] is shown in the bottom panel of Figure 4 (b). The large (40% at its peak) drop in  $P^m$  seen in this figure derives its strength mainly from the resonant enhancement in  $P_e^m$ . Defining  $P = P^m - P^v$  and incorporating the condition that  $E_{res} = E_{peak}^v$  of  $P$  (Eq. 2.16) leads to

$$P = \frac{h}{\sin^2 \sin 2_{13} p} - \frac{i}{2} = 0.25 \sin^2 [\sin 2_{13} p] \quad (2.17)$$

The  $_{13}$  sensitivity of  $P^m$  for  $L = 7000 \text{ Km}$  and for  $L = 9700 \text{ Km}$  is shown in Figure 6. In Figure 6 (a), we see that for  $L = 7000 \text{ Km}$ , the maximum  $_{13}$  sensitivity is in the energy range 4-10 GeV. Here, as in the case of  $P^m$  for  $L = 9700 \text{ Km}$  (Figure 5), the event rate and hence the statistical significance is higher for smaller  $_{13}$ , which allows a probe of even very small values of  $_{13}$  if the criterion

$$N (_{13} = 0) \geq N (_{13}) \geq 3 N (_{13}); \quad (2.18)$$

is satisfied for the muon event rate. However, as seen in Figure 6 (b), while the  $_{13}$  sensitivity of  $P^m$  for  $L = 9700 \text{ Km}$  is higher in the range 4-6 GeV, it is similar to that of  $P_e^m$ , i.e. the event rate gets smaller with decreasing  $_{13}$ . Figure 7 depicts the sensitivity of  $P^m$  to  $_{23}$  for the same distances, showing a similar inverse relation between the survival probability and the value of  $_{23}$ . Note that, for these baselines,  $P$  changes by as much as 20%, for the currently allowed range of  $_{23}$ . A criterion similar to Eq. 2.18 can be applied to these sensitivities in situations where their observability is feasible. This is likely to happen in long baseline experiments with high luminosity sources.

The width of both the effects discussed above for  $P$  is significant, ranging from 7-15 GeV in the first case (Figure 4 (a)) and 4-10 GeV in the second (Figure 4 (b)). We have checked that they persist over a range of baselines (6000 - 10500 Km), making them observationally feasible, as is demonstrated later.

In general the resonance has a width, and this affects observability. Below we give an expression for  $P$  which incorporates the resonance width and

thus quantifies the deviation between  $E_{\text{res}}$  and  $E_{\text{peak}}^{\nu}$  which can exist while still keeping the effect observable. To include the width of the resonance, we write  $A = \sin^2 \theta_{13} (\cos 2\theta_{13} + q \sin 2\theta_{13})$ ; where  $q$  varies from  $-1$  to  $1$ . With this parametrization,

$$\begin{aligned}
 P &= Q + \sin^2 \theta_{13} \left[ 1 - 27 \frac{31L}{E} \right] \sin^2 \theta_{13} \frac{\sqrt{q^2 + 1} - q}{2} \\
 Q &= \sin^2 \theta_{13} \left[ 1 - 27 \frac{31L}{E} \right] \left[ 1 + \sin^2 \theta_{13} \frac{\sqrt{q^2 + 1} + q}{2} \right] \\
 &= [4(q^2 + 1)] \sin^2 \theta_{13} \left[ 1 - 27 \frac{31L}{E} \right] \sin^2 \theta_{13} \frac{\sqrt{q^2 + 1}}{2} \\
 &+ \sin^2 (1 - 27 \frac{31L}{E}): \tag{2.19}
 \end{aligned}$$

Here,  $Q = \left( \frac{\sqrt{q^2 + 1} - q}{2} \right) \left( \frac{\sqrt{q^2 + 1} + q}{2} \right)$ . In obtaining Eq. 2.19 we have approximated  $\cos 2\theta_{13}$ ;  $\cos^2 \theta_{13} \approx 1$ .

#### 2.4 Degeneracies in the determination of oscillation parameters at very long baselines

In our analytic discussion of matter effects on oscillation probabilities, we have used approximate expressions with the solar mass squared difference  $\Delta m_{21}^2$  set to zero. While this is adequate for a broad understanding of matter effects, it is interesting to look at a more accurate picture with  $\Delta m_{21}^2 \neq 0$  and analyze the issue of parameter degeneracies associated with the inclusion of sub-leading effects. In this situation, the determination of neutrino mass and mixing parameters is complicated by the presence of degeneracies in the oscillation probabilities, which are inherent in a three generation analysis due to the presence of the non-zero CP phase  $\theta_{CP}$ . The degeneracies, which have been extensively studied in the literature for baselines less than 3000 Km, are the  $(\theta_{CP}; \theta_{13})$  ambiguity, the sign ( $\theta_{31}$ ) or mass hierarchy degeneracy and the  $(\theta_{23}; \Delta m_{23}^2)$  or atmospheric angle degeneracy, combining to give an overall eight-fold degeneracy [61-64]. It is relevant to discuss briefly the effect of parameter degeneracies in the context of very long baselines, as are considered in this paper.

The analytic treatment of degeneracies is based on approximate expressions for the oscillation probabilities in matter computed by series expansions in the small parameters - the solar mass squared difference  $\Delta m_{21}^2$  and the mixing angle  $\theta_{13}$ . CP trajectory orbits in biprobability space are widely used for depicting degeneracies, and are conventionally plotted using the analytic expressions. For the purposes of the biprobability calculations here, analytic expressions become progressively inadequate beyond 4000 Km, or more precisely, for values of  $L$  and  $E$  such that  $L/E \approx 10^4$  Km/GeV. Additionally, the small  $\theta_{13}$  expansion also fails for relatively large values of  $\theta_{13}$  (near the present CHOOZ bound). In view of this, we have plotted the CP

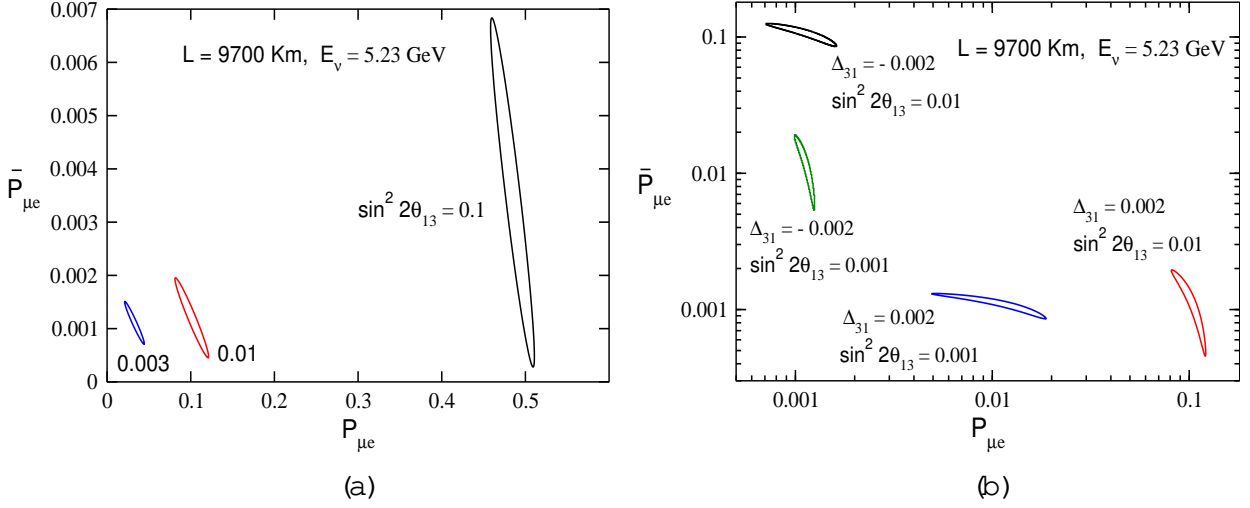


Figure 8: (a) CP trajectory orbits in  $(P_e, P_e)$  biprobability space with  $E = 5.23$  GeV,  $L = 9700$  Km ( $1.27 \sin^2 2\theta_{13} L = E = 3 = 2$ ). Orbits with different values of  $\sin^2 2\theta_{13}$  do not overlap, showing that the  $(\delta_{CP}; \sin^2 2\theta_{13})$  degeneracy is resolved for these values of  $L$  and  $E$ . (b) CP trajectory plots in  $(P_e, P_e)$  biprobability space for two different values of  $\sin^2 2\theta_{13}$  and both signs of  $\delta_{31}$ . Orbits with positive and negative  $\delta_{31}$  do not coincide, showing that the sign  $(\delta_{31})$  degeneracy is resolved for this  $L$  and  $E$  till  $\sin^2 2\theta_{13}$  as low as  $\sin^2 2\theta_{13} = 0.001$ .

trajectories for a sample long baseline using the full numerical solution of the evolution equation with earth matter effects. However, the analytic expressions remain useful for a qualitative understanding of the features and interdependence of parameter degeneracies, and we use them for this purpose whenever necessary.

In general, the expressions for oscillation probability between two flavors, are of the form [63]

$$P = X \cos \delta_{CP} + Y \sin \delta_{CP} + Z ; \quad (2.20)$$

where  $X$ ,  $Y$  and  $Z$  are functions of the neutrino mass squared differences and mixing parameters but independent of the CP phase  $\delta_{CP}$ . Note that  $Z$  contains the dominant contribution to the probabilities given earlier (Eqs. 2.3, 2.4, 2.8, 2.9, 2.13, 2.14). It can be shown that the generic form of a CP trajectory in biprobability space (the orbit traced in  $(P_e, P_e)$  space as  $\delta_{CP}$  varies from 0 to  $2\pi$ ) is an ellipse [63], which collapses to a line under certain conditions.

Here  $P_e$  is the CP conjugated (anti-neutrino) probability. Specific expressions for  $P_e^m$ ,  $P_e^m$  and  $P_e^m$  may be found in [57]. The small  $\delta_{21}$ , small  $\delta_{13}$  series expansions (to second order in these parameters) are compact and hence easier to analyze for degeneracies. Below we list the expressions for the coefficients  $X$  and  $Y$  in this

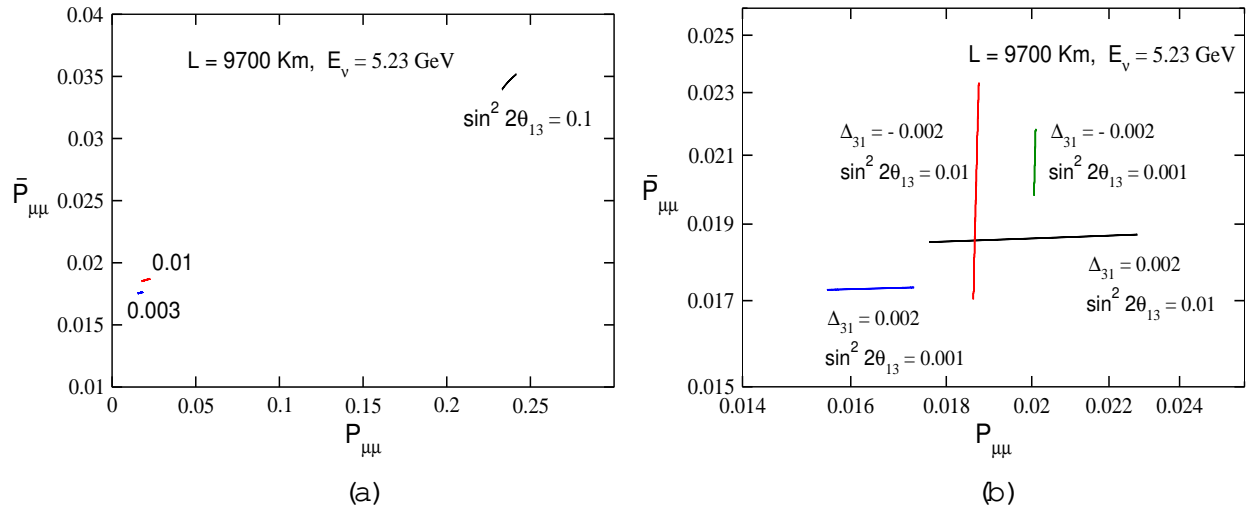


Figure 9: Same as Figure 8(a) and (b) in  $(P_{\mu\mu}, \bar{P}_{\mu\mu})$  biphprobability space. In Figure (b) the  $\text{sign}(\Delta_{31})$  degeneracy is present for  $\sin^2 2\theta_{13} = 0.01$ .

approximation for  $P_e^m$  and  $P^m$ .

$$\begin{aligned}
 X_e &= 2 \sin^2 \theta_{13} \sin^2 2\theta_{12} \sin^2 2\theta_{23} \cos \frac{\sin \hat{A}}{\hat{A}} \frac{\sin(\hat{A}-1)}{(\hat{A}-1)} \\
 Y_e &= 2 \sin^2 \theta_{13} \sin^2 2\theta_{12} \sin^2 2\theta_{23} \sin \frac{\sin \hat{A}}{\hat{A}} \frac{\sin(\hat{A}-1)}{(\hat{A}-1)} \\
 X &= \frac{2}{\hat{A}-1} 2 \sin^2 \theta_{13} \sin^2 2\theta_{12} \sin^2 2\theta_{23} \cos 2\theta_{23} \sin \left[ \hat{A} \sin \frac{\sin \hat{A}}{\hat{A}} \cos(\hat{A}-1) \right] \\
 Y &= 2 \sin^2 \theta_{13} \sin^2 2\theta_{12} \sin^2 2\theta_{23} \sin \frac{\sin \hat{A}}{\hat{A}} \frac{\sin(\hat{A}-1)}{(\hat{A}-1)} \quad (2.21)
 \end{aligned}$$

where  $\hat{A} = 1.27 \theta_{31} L = E$ ,  $\hat{A} = A = j_{31} j_{21} j_{31}$ . The above expressions are for the normal mass hierarchy. For the inverted hierarchy, the transformations  $\hat{A} \rightarrow -\hat{A}$ ,  $\theta_{12} \rightarrow \theta_{12} + \pi$  and  $\theta_{23} \rightarrow \theta_{23} + \pi$  are required. The coefficients for  $P^m$  are given by  $X = X_e - X$ , and similarly for  $Y$ . Note that  $Y = 0$  and hence the survival probability is independent of the CP-odd term. Next we discuss in turn each of the possible degeneracies.

The  $(C_P; \theta_{13})$  degeneracy arises when different pairs of values of the parameters  $C_P$  and  $\theta_{13}$  give the same neutrino and anti-neutrino oscillation probabilities,

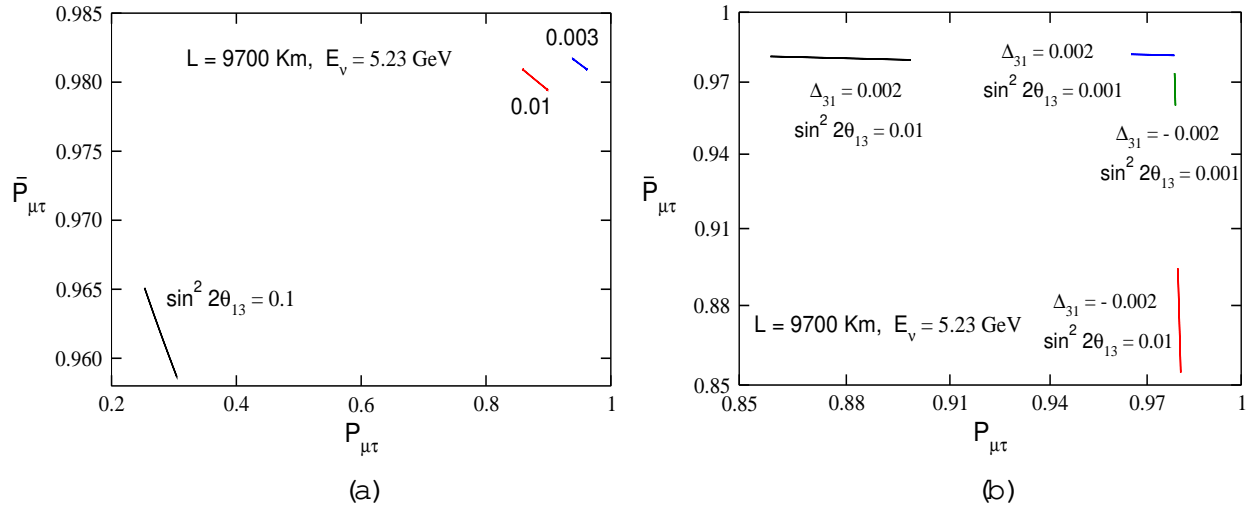


Figure 10: Same as Figure 8 (a) and (b) in  $(P_{\mu\tau}, \bar{P}_{\mu\tau})$  biprobability space.

assuming other parameters to be known and fixed. This may be expressed as

$$\begin{aligned}
 P_{\mu\tau}(C_P; \theta_{13}) &= P_{\mu\tau}^0(C_P; \theta_{13}) \\
 \bar{P}_{\mu\tau}(C_P; \theta_{13}) &= \bar{P}_{\mu\tau}^0(C_P; \theta_{13})
 \end{aligned}
 \quad (2.22)$$

This ambiguity manifests itself in the intersection of CP orbits with different values of  $\theta_{13}$ . The intersection points indicate the different values of  $C_P$  and  $\theta_{13}$  for which the above Eqs. 2.22 are satisfied. For values of  $L$  and  $E$  such that  $\Delta_{31} = n\pi = 2\pi$ , Eqs. 2.21 predict that either  $\sin C_P$  or  $\cos C_P$  drops out of the expression for  $P_{\mu\tau}^m$ , reducing the CP trajectory to a straight line. Further, it can be shown that the  $(C_P; \theta_{13})$  ambiguity reduces in this case to a simple  $(C_P; \theta_{13})$  or  $(C_P; 2\theta_{13})$  ambiguity which does not mix different values of  $\theta_{13}$  [62]. This fact holds true at long baselines also, as is depicted in Figure 8 (a) for  $L = 9700 \text{ Km}$ ,  $E = 5.23 \text{ GeV}$  (giving  $\Delta_{31} = 3\pi = 2\pi$ ). Here the CP orbits appear as widely separated narrow ellipses, showing that the  $(C_P; \theta_{13})$  ambiguity is effectively resolved<sup>6</sup>. CP orbit diagrams for  $P_{\mu\tau}^m$  and  $\bar{P}_{\mu\tau}^m$  are given in Figure 9 (a) and 10 (a), illustrating a similar lifting of the degeneracy involving  $\theta_{13}$  in both cases. The approximate expressions (Eq. 2.21) show that the muon neutrino survival probability is a function only of the CP-even term  $\cos C_P$ , while  $\bar{P}_{\mu\tau}^m$  only depends on  $\sin C_P$  when  $\theta_{23}$  is maximal, so their CP orbits resemble straight lines instead of ellipses.

<sup>6</sup>Here we have given a theoretical discussion of degeneracies in probabilities, and therefore not taken into account possible error bars in the experimental results for event rates, which, if large enough, may cause points on different  $\theta_{13}$  orbits to overlap.

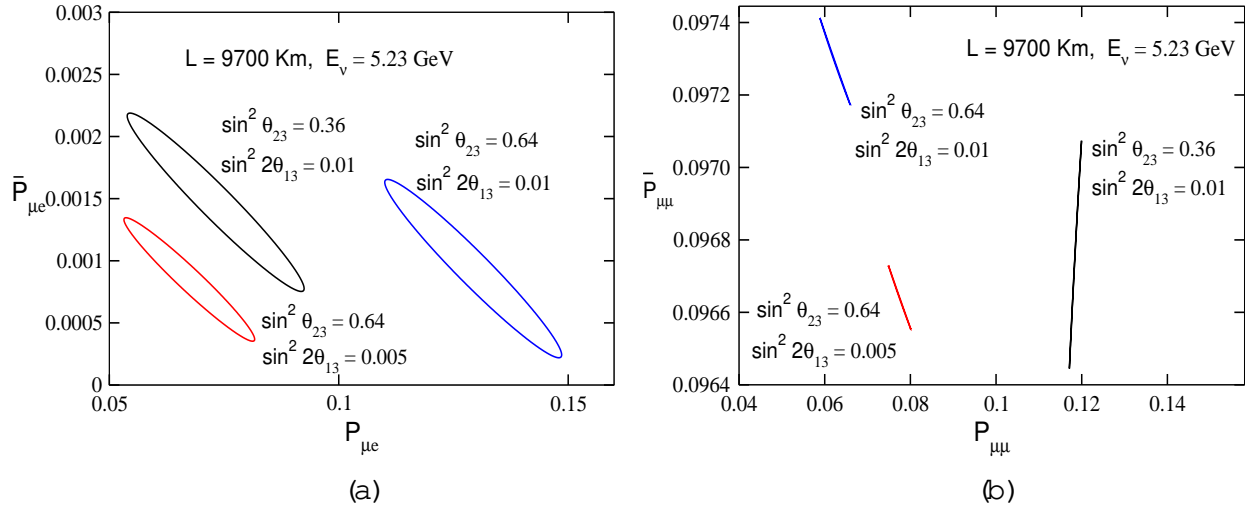


Figure 11: (a) CP trajectory plots in  $(P_e, P_e)$  biphprobability space for di erent values of  $\theta_{23}$  and complementary values of  $\theta_{13}$ . (b) Same as Figure 11 (a) in  $(P_\mu, P_\mu)$  biphprobability space.

The mass hierarchy degeneracy occurs due to identical solutions for  $P$  and  $\bar{P}$  for di erent pairs of  $\theta_{CP}$  and  $\theta_{13}$  with opposite signs of  $\theta_{31}$  (again fixing other parameters):

$$\begin{aligned} P(\theta_{31} > 0; \theta_{CP}; \theta_{13}) &= P(\theta_{31} < 0; \theta_{CP}^0; \theta_{13}^0) \\ P(\theta_{31} > 0; \theta_{CP}; \theta_{13}) &= P(\theta_{31} < 0; \theta_{CP}^0; \theta_{13}^0) \end{aligned} \quad (2.23)$$

Note that a combined effect of the  $(\theta_{CP}; \theta_{13})$  ambiguity and the  $\text{sign}(\theta_{31})$  degeneracy gives rise to a four-fold degeneracy. From the expression for  $P_{\mu e}^m$ , it has been determined [62] that the condition for this ambiguity to be resolved is

$$\sin 2\theta_{13} > \frac{2 \tan \theta_{23} \sin 2\theta_{12} \sin \hat{A}}{\hat{A} \left[ \frac{\sin(1-\hat{A})}{1-\hat{A}} - \frac{\sin(1+\hat{A})}{1+\hat{A}} \right]} \quad (2.24)$$

This places constraints on  $\theta_{13}$  as well as the baseline, which must be large enough for the denominator to be large (thus weakening the constraint on  $\theta_{13}$ ). Figure 8 (b) gives the orbit diagram for the energy and baseline earlier discussed. It is seen that the orbit ellipses for positive and negative  $\theta_{31}$  are well-separated for  $\sin^2 2\theta_{13} = 0.001$ . Thus the degeneracy is lifted even for very small values of  $\theta_{13}$ . From Figure 10 (b), it is clear that  $P^m$  is also free from this ambiguity for large baselines. However,  $P^m$  shows a mass hierarchy degeneracy for  $\sin^2 2\theta_{13} = 0.01$ , as seen in Figure 9 (b).

Currently  $\theta_{23}$  is determined from  $P^\nu$  in atmospheric (Super-K) and accelerator (K2K) experiments. Since this is a function of  $\sin^2 2\theta_{23}$ , these measurements

cannot differentiate  $\theta_{23}$  from  $\theta_{23} = 2\theta_{23}$ . If the probability is a function of  $\sin^2 \theta_{23}$  or  $\cos^2 \theta_{23}$  (e.g. the leading contributions in  $P_{e\mu}$  and  $P_{e\tau}$  respectively), then for a fixed value of  $\theta_{13}$ ,  $P_{\mu\tau}(\theta_{23}; \theta_{13}) \neq P_{\mu\tau}(\theta_{23} = 2\theta_{23}; \theta_{13})$ . However, different values of  $\theta_{13}$  and the CP phase  $\delta_{CP}$  can make them equal<sup>7</sup>, leading to an ambiguity in the determination of the latter two parameters known as the  $(\theta_{23}; \theta_{23} = 2\theta_{23})$  degeneracy:

$$\begin{aligned} P_{\mu\tau}(\theta_{23}; \delta_{CP}; \theta_{13}) &= P_{\mu\tau}(\theta_{23} = 2\theta_{23}; \delta_{CP}^0; \theta_{13}^0) \\ P_{\mu\tau}(\theta_{23}; \delta_{CP}; \theta_{13}) &= P_{\mu\tau}(\theta_{23} = 2\theta_{23}; \delta_{CP}^0; \theta_{13}^0) \end{aligned} \quad (2.25)$$

The presence of this ambiguity along with the two previously discussed degeneracies will give rise to an eight-fold degeneracy [62] in such probabilities. However, if a probability is a function of  $\sin^2 2\theta_{23}$  (e.g.  $P_{\mu\tau}$ ), then for a fixed  $\theta_{13}$ ,  $P_{\mu\tau}(\theta_{23}; \theta_{13}) = P_{\mu\tau}(\theta_{23} = 2\theta_{23}; \theta_{13})$  to start with. Therefore, different values of  $\theta_{13}$  and  $\delta_{CP}$  give rise to different values of the probability, and the  $(\theta_{23}; \theta_{23} = 2\theta_{23})$  degeneracy will not lead to any further ambiguity in the determination of  $\theta_{13}$ . So the total degeneracy in this case is four-fold<sup>8</sup>.

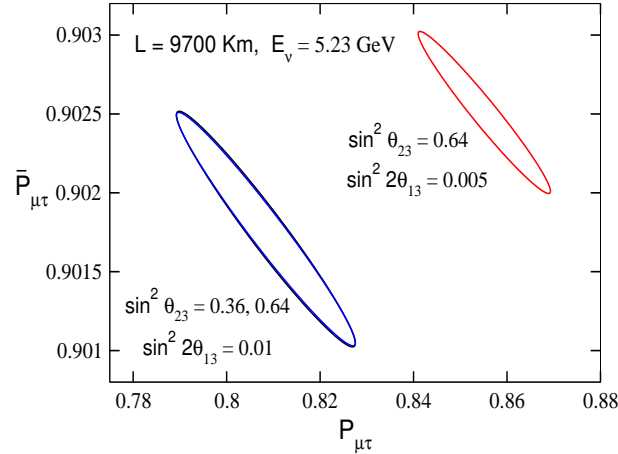


Figure 12: Same as Figure 9(a) in  $(P_{\mu\tau}, \bar{P}_{\mu\tau})$  biphprobability space.

The CP trajectories for  $P_{e\mu}^m$ ,  $P_{e\tau}^m$  and  $P_{\mu\tau}^m$  with complementary values of  $\theta_{23}$  and our sample L and E are given in Figure 11(a) and (b) and Figure 12.

<sup>7</sup>This degeneracy may be present even if  $\delta_{CP} = 0$ .

<sup>8</sup>Note that probabilities that are functions of  $\sin^2 2\theta_{23}$ , though only 4-fold degenerate with respect to  $\theta_{13}$  and  $\delta_{CP}$ , cannot ascertain whether  $\theta_{23} < \theta_{23} = 4$  or  $\theta_{23} > \theta_{23} = 4$ . This information can be obtained from a comparison of probabilities which are functions of  $\sin^2 \theta_{23}$  and  $\cos^2 \theta_{23}$  (e.g. the golden and silver channels discussed in [65,66]).

From Figure 11 (a) and (b), we see that the different  $\theta_{23}$  orbits do not intersect, i.e. this degeneracy is resolved in  $P_e^m$  and  $P^m$  for a long baseline like the one discussed, even though in principle it could exist for these probabilities as they are functions of  $\sin^2 \theta_{23}$ . However, in the case of  $P^m$ , as discussed above, this degeneracy is absent since its approximate matter expression contains only  $\sin^2 2\theta_{23}$  in its dominant terms. This feature is evident in Figure 12. We see that all points on the orbits with complementary  $\theta_{23}$  and equal  $\delta_{13}$  coincide, so no two independent values of  $\delta_{CP}$  can exist which give the same probability.

It can also be observed from the analytic expressions for  $X$  and  $Y$  (Eq. 2.21) that the magic baseline scenario [67] discussed for  $P_e^m$  is equally valid for  $P^m$  and  $P^m$  when  $\theta_{23} = \pi/4$ . This method of degeneracy resolution requires the baseline to satisfy  $\hat{A} = \pi$ , in which case all coefficients of  $\delta_{CP}$  vanish. The energy and parameter-independent condition on  $L$  becomes  $\delta_{av}L = 32532 \text{ Km gm/cc}$ . From the  $\delta_{av}L$  vs  $L$  curve (Fig 1), it is seen that this corresponds to  $L = 7600 \text{ Km}$ . An identical analysis applies to  $P^m$  and  $P^m$  with maximal  $\theta_{23}$ , with only a small correction if  $\theta_{23}$  is non-maximal.

In conclusion, we find that a study of probabilities at a baseline and energy like the one discussed demonstrates, in general, a breaking of most of the parameter degeneracies which can confuse the determination of  $\theta_{13}$  from oscillation measurements. For  $P_e$ , this is true for all three classes of degeneracies mentioned above. In the case of the muon survival probability, Fig 9 (b) shows that  $\text{sign}(\delta_{31})$  may still be undetermined for specific values of  $\theta_{13}$  and the CP phase  $\delta_{CP}$ , for which the same value of  $(P_{\mu}, P_{\nu})$  are obtained with opposite signs of  $\delta_{31}$ . For example, for  $\sin^2 2\theta_{13} = 0.01$ , we have checked that  $\delta_{CP} = 0.305$  and  $\delta_{CP} = 0.337$  give the same point in  $(P_{\mu}, P_{\nu})$  space for positive and negative  $\delta_{31}$  respectively for  $L = 9700 \text{ Km}$  and  $E = 5.23 \text{ GeV}$ . In  $P^m$ , all degeneracies involving a measurement of  $\theta_{13}$  and  $\delta_{CP}$  are lifted for the energy and baseline discussed. Also, we note that the maximum total degeneracy of  $P^m$  is four-fold even in principle, since its analytic expression in matter (to second order in the expansion parameters) is a function of  $\sin 2\theta_{23}$ .

### 3. Determining the Mass Hierarchy via Atmospheric $\nu_{\tau}$ in a charge discriminating Detector

In the discussion in Sections 2.1-2.3, we have made an effort to show that large matter effects in neutrino oscillations are not necessarily connected to  $\nu_e \rightarrow \nu_e$  conversions, but can be searched for in  $\nu_e \rightarrow \nu_{\mu}$  oscillation and  $\nu_e$  survival probabilities. We have examined their origin by studying the inter-relations

of all the three matter probabilities,  $P_e^m$ ,  $P^m$  and  $P^m$ , and identified baseline and energy ranges where they act coherently to give observationally large effects. The effects discussed are strongly sensitive to the sign of  $\theta_{31}$ , as is apparent in the figures above. It is useful to recall Eq. 2.15 and emphasize that contrary to what one generally assumes,  $P$  is not necessarily negative, i.e.  $P^m$  is not always less than or equal to  $P^v$ . This would be true if large matter effects resided only in  $P_e^m$ , since  $P_e$  is positive over the relevant range of energies and baselines. However, as shown earlier, matter effects can not only lead to a substantial enhancement of  $P_e^m$ , but can also cause an appreciable drop or rise in  $P^m$ , i.e.  $P$  can be large. Depending on the extent of this,  $P^m$  may be larger or smaller than  $P^v$ . Specialized detectors operating in long baseline scenarios with high luminosity sources should be able to observe effects like the one discussed in relation to the central panel of Figure 4 (a) above via appearance events. An intense source [37] would be required because the effects are manifested at energies which, while above the tau production threshold, are still close enough to it so that the CC cross-section is relatively small. A study of this will be reported elsewhere [68]. For the present, using the fact that matter effects in  $P^m$  and  $P_e^m$  translate into matter effects in  $P^m$ , we focus on the detection of muon and anti-muon survival rates in atmospheric neutrinos.

Atmospheric neutrinos, while not a controlled source in the sense of the beam experiments described above, offer a compensating advantage: a very broad L/E band extending about 5 orders of magnitude (1 to  $10^5$  Km/GeV, with neutrino energies,  $E \geq 1$  GeV and above, L from a few Km to about 12500 Km). The longer baseline lengths allow matter effects to develop [69], and offer possibilities for determination of the mass hierarchy using a detector capable of identifying muon charge. Other physics possibilities with a charge discriminating detector using either atmospheric neutrinos or a neutrino beam as source have been discussed in [37,70-72].

Prior to giving the results of our calculations, we briefly describe some of the inputs we have used. The prototype for our calculations is a 100 kT Iron detector, with detection and charge discrimination capability for muons provided by a magnetic field of about 1.2 Tesla. Sensitive elements are assumed to be Glass Spark Counters (RPC). We have assumed a (modest) 50% efficiency of the detector for muon detection. The L/E resolution will depend on event kinematics and on muon track detection capabilities<sup>9</sup>. In the calculations presented here, we have used the Bartol [73] atmospheric flux and set a muon detection threshold of 2 GeV. These specifications have been culled from the MONOLITH [74] and INO [75] proposals and hence are realistic to the best of our knowledge.

In order to demonstrate the important qualitative features of our results, we have selectively provided both tables of event rates as well as plots versus L and

---

<sup>9</sup>For our study, we do not use any resolution function. For the most part in what follows, we draw our conclusions based on event rates summed over fairly large ranges in L and/or E.

E (GeV)	2-3	3-5	5-7	7-10	2-10
L (Km)	m at vac				
2000-4000	99, 102	37, 41	11, 12	23, 23	170, 178
4000-6000	55, 59	92, 93	17, 19	3, 3	167, 174
6000-8000	71, 71	47, 48	45, 45	10, 12	173, 176
8000-9700	49, 49	47, 48	27, 25	22, 23	145, 145
9700-10500	25, 26	20, 21	6, 5	12, 13	63, 65
10500-12500	60, 58	54, 55	10, 11	27, 26	151, 150
2000-12500	359, 365	297, 306	116, 117	97, 100	869, 888

Table 2: Integrated  $\nu_{\mu}$  events in matter and in vacuum in restricted bins of E and L for  $\theta_{31} = 0.002 \text{ eV}^2$  and  $\sin^2 2_{13} = 0.1$ .

L/E for positive  $\theta_{31}$ . Atmospheric neutrinos offer the advantage of being able to appropriately select ranges in L and E from a large spectrum of L and E values.

An approximate feel for where significant matter effects are likely to show up in muon survival rates can be obtained using our earlier discussion in Sections 2.1-2.3, especially that which leads to Eqs. 2.6, 2.7, 2.10 and 2.16. In particular, the resonance condition (Eq. 2.6) gives the following constraint on the product of density and energy:

$$E_{\text{res}} = 1.315 \cdot 10^4 \cdot \theta_{31} \cos 2_{13} \text{ GeV gm/cc} \quad (3.1)$$

From Eq. 3.1, using the value  $\theta_{31} = 0.002 \text{ eV}^2$  and approximating to the case of a constant average density  $\rho_{\text{av}}(L)$  for any given baseline, one obtains the expression<sup>10</sup>

$$\rho_{\text{av}}(L) E_{\text{res}} = 25 \text{ GeV gm/cc} \quad (3.2)$$

In Figure 13, we plot  $\rho_{\text{av}}(L)$  vs L for the earth. A rough measure of  $E_{\text{res}}$  for any given baseline may thus be obtained using this plot and Eq. 3.2. This is also useful in

<sup>10</sup>Note that the resonance condition is not very sensitive to the value of  $\theta_{13}$ , since the dependence is through a cosine. However, it does depend on what value of  $\theta_{31}$  we use. For example, for  $\theta_{31} = 0.002 \text{ eV}^2$ ,  $E_{\text{res}} = 26.3 \cos 2_{13}$ , which gives  $E_{\text{res}} = 24.96$  for  $\sin^2 2_{13} = 0.1$  and  $E_{\text{res}} = 26.18$  for  $\sin^2 2_{13} = 0.01$ ; however, for  $\theta_{31} = 0.0015 \text{ eV}^2$ ,  $E_{\text{res}} = 19.7 \cos 2_{13}$ , giving  $E_{\text{res}} = 18.7$  for  $\sin^2 2_{13} = 0.1$ .

E (GeV)	2 - 3	3 - 5	5 - 7	7 - 10	2 - 10
L (Km) +	m at vac				
2000 - 4000	229, 233	99, 93	31, 28	55, 53	414, 407
4000 - 6000	134, 139	191, 215	42, 45	10, 8	377, 407
6000 - 8000	168, 169	115, 113	81, 109	21, 30	385, 421
8000 - 9700	120, 118	129, 115	59, 63	43, 59	351, 356
9700 - 10500	63, 62	39, 51	24, 13	29, 32	155, 158
10500 - 12500	136, 138	118, 138	29, 28	70, 69	353, 373
2000 - 12500	850, 859	691, 725	266, 287	228, 251	2035, 2122

Table 3: Integrated  $\mu$  events in matter and in vacuum in restricted bins of E and L for  $\theta_{31} = 0.002$  eV<sup>2</sup> and  $\sin^2 2\theta_{13} = 0.1$  (see text for details).

understanding the broad features of the tables representing our actual calculations, and in selecting baseline and energy ranges for closer scrutiny, even though the constant density approximation fails once baselines are very long.

We now proceed with the discussion of our event rate calculations which, as stated earlier, have been performed by solving the full three flavour neutrino propagation equation using the PREM [58] density profile of the earth. We have scanned the energy range 2-10 GeV<sup>11</sup> and the L range of 2000-12500 Km for evidence of matter effects. We have assumed  $\theta_{21} = 8.3 \times 10^{-5}$  eV<sup>2</sup>,  $\sin^2 \theta_{12} = 0.27$  [17],  $\theta_{CP} = 0$  and an exposure of 1000 kT-yr for the tables and all plots. Note that for baselines > 10500 Km, passage is through the core of the earth.

In Table 2, we show the  $\mu$  event rates in matter and in vacuum integrated over various energy and baseline bins. As expected, matter effects are negligible for antimuons if  $\theta_{31}$  is positive.

Table 3 shows the integrated atmospheric rates for the same bin choices, but for muons. We note that while there are visible differences between matter

<sup>11</sup>Higher values of energies are also possible, but the flux factor considerably diminishes the event rates. Therefore we take E upto 10 GeV only.

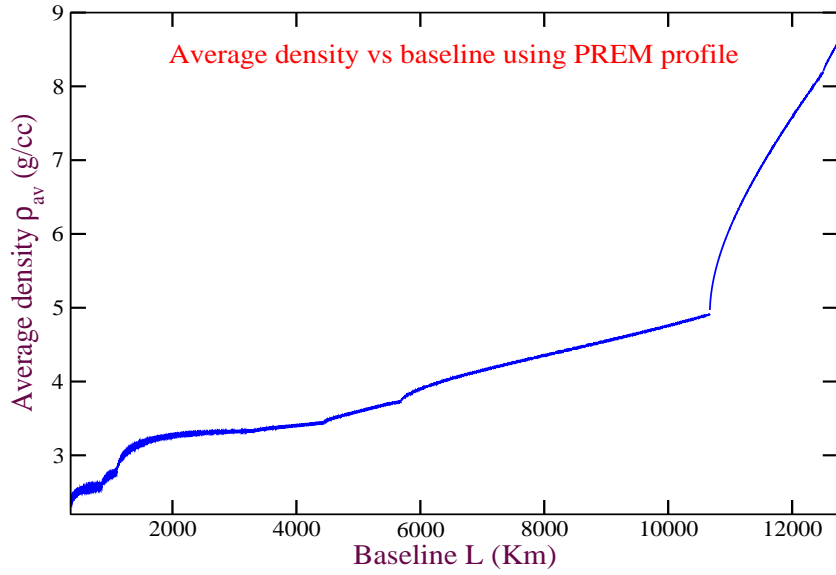


Figure 13: The average density  $\rho_{av}$  for each baseline  $L$ , obtained from the PREM (Preliminary Reference Earth Model) density profile, plotted vs  $L$ .

$L = 6000$  to  $9700$  Km,  $E = 5$  to  $10$  GeV

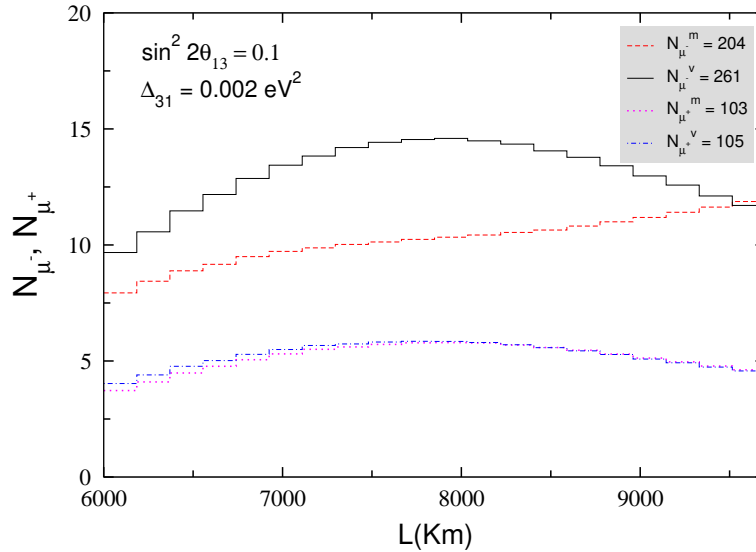


Figure 14: Atmospheric muon and anti-muon events plotted against  $L$  for energy range of 5 GeV to 10 GeV and baselines between 6000 Km to 9700 Km. The numbers in the legend correspond to the integrated number of muon and anti-muon events for the restricted range of  $L$  and  $E$  in matter and in vacuum for a given value of  $\sin^2 2\theta_{13}$ .

and vacuum rates, they are not always significantly large. A careful selection of energy ranges and baselines is necessary to extract a statistically significant signal. Our plots below reflect these selections. In particular, in Table 3, a

4 signal for matter effects can be extracted from the energy bins 5-10 GeV and the L bins 6000-9700 Km (shown in bold text in the table), as discussed below. Consolidating the event rates over large bins in energy and baseline will lead to a dilution, or possibly a wash-out of the signal, as is evident from this table. For example, the right-most vertical column shows the energy integrated events for the range 2-10 GeV and the last row lists the events integrated over the 2000-12500 Km baseline range. In both cases, one notes a dilution of the signal for matter effects. We also note that except in the energy range 3-5 GeV, matter effects in the core are not appreciable. These effects may be looked for in higher luminosity beam experiments.

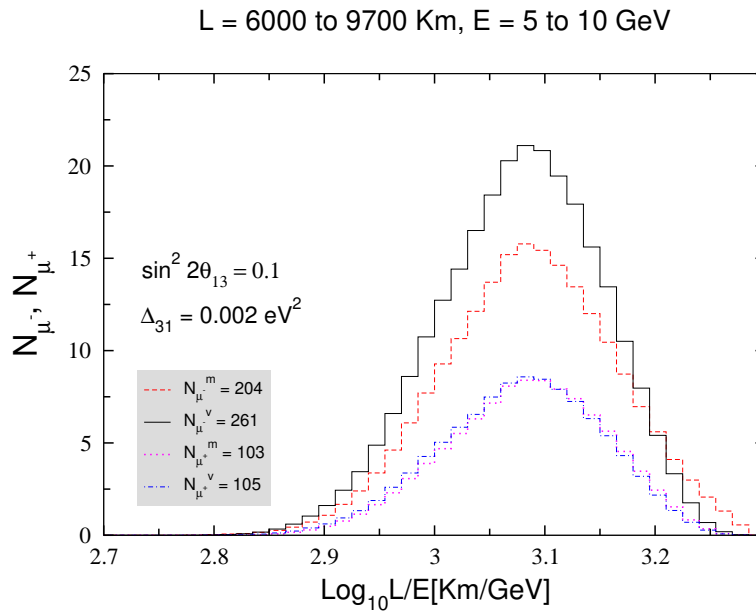


Figure 15: The total event rate for muons and antimuons in matter and in vacuum plotted against  $\text{Log}_{10}(L/E)$  for the restricted choice of L and E range (see Figure 14). The numbers in the legend correspond to the integrated number of muon and antimuon events for the restricted range of L and E in matter and in vacuum for a given value of  $\sin^2 2\theta_{13}$ .

In Figure 14 we show event rates for muons and antimuons versus L for the baseline and energy bins mentioned above ( $L = 6000-9700 \text{ Km}$ ,  $E = 5-10 \text{ GeV}$ ). We have assumed  $\Delta_{31} = 0.002 \text{ eV}^2$  and  $\sin^2 2\theta_{13} = 0.1$  for this plot. The effect is large for this choice of energies and baselines because it is a combination of the two effects visible in the bottom panels of Figure 4. The fall in  $P^m$  at 9700 Km between 6-15 GeV (which persists over a range of baselines) obtains a large contribution from  $P^m$  while the effect shown at 7000 Km arises primarily due to  $P_e^m$ . Both work to lower the muon survival rate below its vacuum value. In contrast to an expected vacuum oscillation rate of 261 events, one expects 204 events if the sign of  $\Delta_{31}$  is positive, which has a statistical significance of 4.

Figure 15, for the same energy/baseline ranges and parameter values shows the event distributions for muons and antimuons versus  $L/E$ .

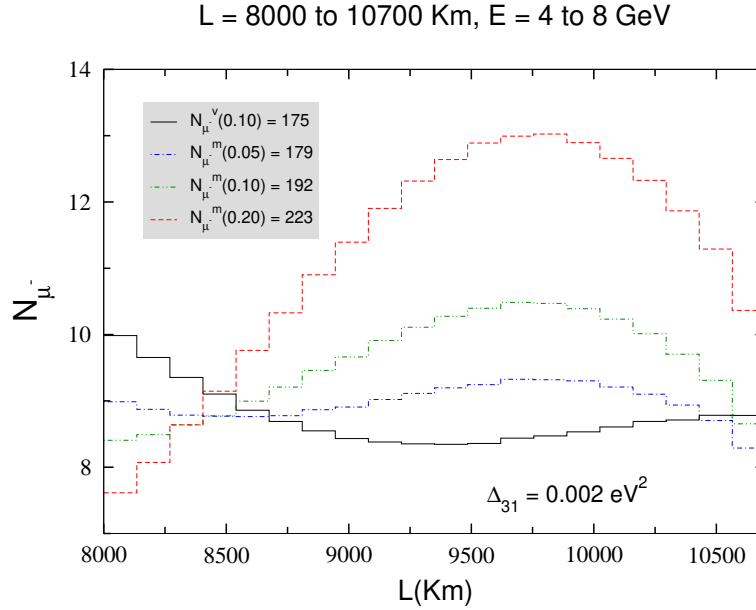


Figure 16: Atmospheric muon events plotted against  $L$  for energy range of 4 GeV to 8 GeV and baselines between 8000 Km to 10700 Km. The numbers in the legend correspond to the integrated number of muon events for the restricted range of  $L$  and  $E$  in matter and in vacuum for various values of  $\sin^2 2_{13}$  (in parenthesis).

As an example of how the muon survival rate can rise above the expected vacuum value, we show in Figure 16 the muon event rate for the baseline range of 8000–10700 Km and the energy range of 4–8 GeV. The solid curve is the vacuum event rate for  $\sin^2 2_{13} = 0.1$ , while the three others are the muon survival rates incorporating matter effects for values of  $\sin^2 2_{13} = 0.05, 0.1$  and  $0.2$  respectively<sup>12</sup>. The curves exhibit the rise above the vacuum survival rate visible in the energy range 4–7 GeV in the bottom panel of Figure 4 (a). In addition, the curves demonstrate the sensitivity to  $\theta_{13}$  which is exhibited in the probability plot given in Figure 6 (b) in the energy range 4–7 GeV. For values of  $\sin^2 2_{13}$  close to the present CHOOZ bound, a  $> 3\sigma$  signal from matter effect is visible in Figure 16. Values of  $\sin^2 2_{13}$  appreciably lower than this would necessitate a high luminosity source (e.g. neutrino factory) or a higher exposure time with atmospheric neutrinos for conclusive observation. A similar  $\theta_{13}$  sensitivity cum event rate plot is also given in Figure 17 with the muon rate now plotted versus  $L/E$ . Here it is seen that  $N_{\mu}$  is particularly sensitive to  $\theta_{13}$

<sup>12</sup>Note that the vacuum curve will not change appreciably with a change in  $\theta_{13}$ , so it serves as the reference plot for vacuum.

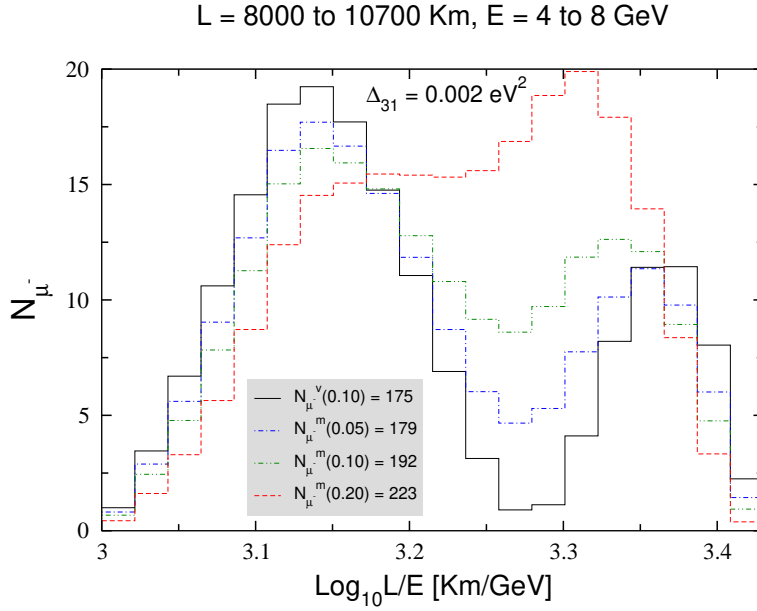


Figure 17: The total event rate for muons in matter and in vacuum plotted against  $\text{Log}_{10}(L=E)$  for the restricted choice of  $L$  and  $E$  range (see Figure 16). The numbers in the legend correspond to the integrated number of muon events for the restricted range of  $L$  and  $E$  in matter and in vacuum for various values of  $\sin^2 2_{13}$  (in parenthesis).

in the range  $3.2 - 3.35$  of  $\text{Log}_{10}(L=E)$ , where there is a significant difference between the vacuum and matter values even for  $\sin^2 2_{13} = 0.05$ . This may be looked for provided the  $L/E$  resolution is sufficient to observe this. We note that a significant rise of the muon survival rate in matter over its vacuum values is a signal of the size of the matter effect in  $P_{ee}$  overcoming that due to  $P_{e\mu}$ , in spite of the fact that the latter is close to resonance values (Figure 4 (a), in the energy range 4–7 GeV).

Further demonstration of the sensitivity to the sign of  $\delta_{31}$  and of the effects discussed in this paper can be gleaned from plots of the ratio of muon to anti-muon event rates  $[N_{\mu^-} = N_{\mu^+}]$ . In Figure 18 (a) we show this ratio for the baseline range 6000–9700 Km and the energy range 5–20 GeV. The dominant effect here is due to the reduction in  $P^{mm}$  stemming from a large enhancement of  $P_{e\mu}^m$ , (as evident in the probability plots for 7000 Km in Figure 4 (b) above) and this is clearly visible in the event rates. Comparing the curves for positive and negative  $\delta_{31}$ , we see that the peak to peak difference between them is about 90%.

Selecting different (lower) ranges in both baselines and energy, we show the rate ratio for 4000 – 9000 Km and 3 – 10 GeV in Figure 18 (b). As evident from the discussion of the previous section, the  $P^m$  effects develop after 8000 Km for

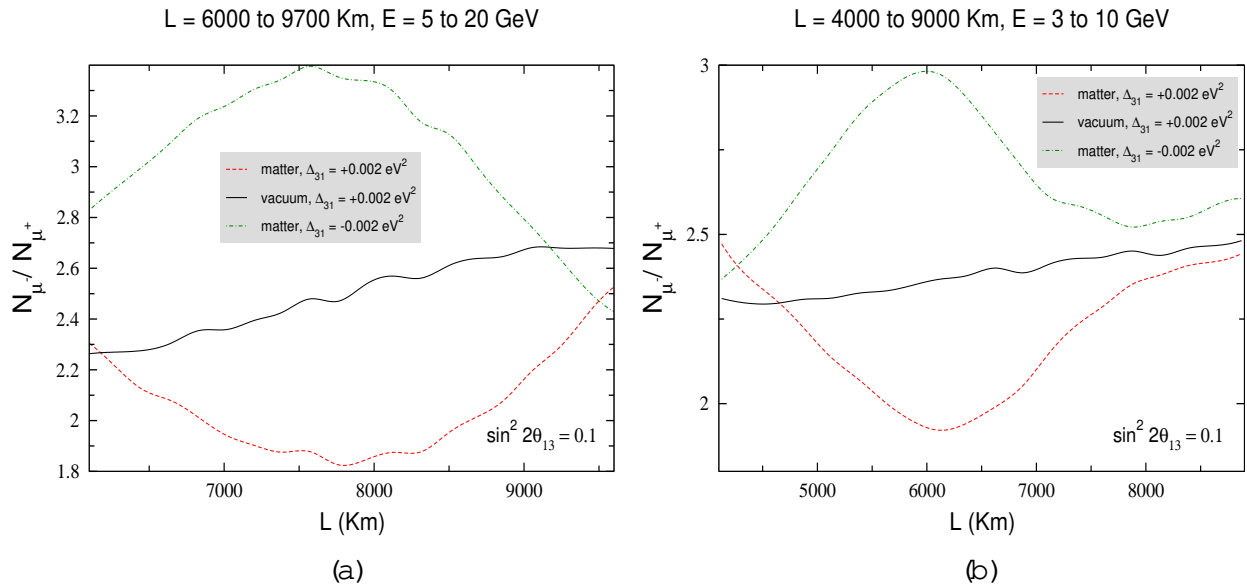


Figure 18: (a) Ratio of atmospheric muon and antimuon events plotted against L for energy range of 5 GeV to 20 GeV and baselines between 6000 Km to 9700 Km . (b) Ratio of atmospheric muon and antimuon events plotted against L for energy range of 3 GeV to 10 GeV and baselines between 4000 Km to 9000 Km .

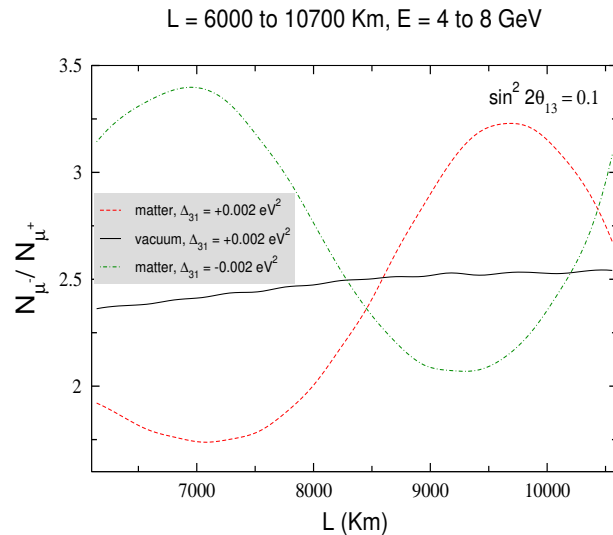


Figure 19: Ratio of atmospheric muon and antimuon events plotted against L for energy range of 4 GeV to 8 GeV and baselines between 6000 Km to 10700 Km .

the most part, hence this choice is primarily suited to demonstrate the effect of  $P_e^m$  on  $P^m$  . The influence of  $P^m$  is, however, visible at the higher baselines, as it draws the  $\Delta_{31} > 0$  curve close to the vacuum curve because, as discussed above, the  $P_e^m$  and  $P^m$  effects work in the opposite direction in this region. The dip-peak separation for the curves for  $\Delta_{31} > 0$  and  $\Delta_{31} < 0$  is about 60%

in this case.

Finally, in an attempt to show an example of a baseline/energy range where both effects, i.e. the effect where  $P^m$  plays a major role by raising the rate ratio above its vacuum value, and the effect where the resonant rise in  $P_e^m$  dominates over  $P^m$  to bring about a decrease in  $N_{\nu} = N_{\nu} +$  compared to its value in vacuum, we choose the baseline range 6000–10700 Km and the energy range 4–8 GeV (Figure 19). For  $\theta_{31} > 0$ , the dip in the ratio is maximum around 7000 Km and originates from the drop in the probability visible in the bottom panel of Figure 4 (b), while the rise above the vacuum curve, which is maximum around 9700 Km, is a manifestation of the increase in  $P$  consequent to the large decrease in  $P$  occurring in the range 4–8 GeV, shown in Figure 4 (a).

#### 4. Conclusions

To conclude, we summarize the salient points of our study:

In addition to  $P_e$ , interesting and appreciable matter effects can arise in  $P$  at baselines  $> 7000$  Km. These can synergistically combine to give correspondingly large effects in  $P^m$ . As a result, observably large signals may appear in a charge discriminating detector capable of measuring muon survival rates, providing a handle on the sign of  $(\theta_{31})$ .

Both  $P^m$  and  $P_e^m$  are sensitive to  $\theta_{13}$ . We have identified baselines and energies where this sensitivity is high and in particular, where the probabilities tend to increase as  $\theta_{13}$  decreases, facilitating the determination of small values of  $\theta_{13}$  with a greater statistical significance. We have also studied the  $\theta_{23}$  dependence of  $P^m$  and  $P_e^m$ .

We have performed a detailed study of parameter degeneracies at very long baselines, using numerical results with a realistic earth density profile. We find that for these baselines and at energies for which the criterion  $1.27 \theta_{31} L = E = m_{\nu}^2 = 2$  is satisfied,  $P_e^m$  is largely free of the degeneracies which could obscure measurements of  $\theta_{13}$  and  $\text{sign}(\theta_{31})$ . The  $(\theta_{CP}; \theta_{13})$  degeneracy is lifted for  $P^m$  and  $P_e^m$  also. The  $\text{sign}(\theta_{31})$  degeneracy vanishes for  $P^m$  at such baselines and energies, but can be present in  $P_e^m$  for some specific values of  $\theta_{13}$  and  $\theta_{CP}$ . We also note that the determination of  $\theta_{13}$  from  $P^m$  does not suffer from the  $(\theta_{23}, \theta_{23} = 2 - \theta_{23})$  degeneracy,  $P^m$  being a function of  $\sin 2\theta_{23}$ . Further, for the baselines and energies relevant for us this degeneracy disappears from  $P^m$  and  $P_e^m$  as well.

In the second part of the paper we perform detailed calculations of muon survival rates for atmospheric neutrinos, using a 100 kT charge-discriminating

iron calorimeter as prototype. Our choice here is guided by our motivation to explore whether it is possible to realistically determine the sign of  $\theta_{31}$  in an atmospheric neutrino experiment, over a timescale shorter than that anticipated for neutrino factories.

While atmospheric neutrinos make available a wide range of baselines and energies, we find that in order to detect matter effects a careful screening and selection of  $L$  and  $E$  is necessary to overcome the lack of a high intensity beam. We use our earlier discussion of matter effects in  $P_e^\mu, P^\mu$  and  $P^\mu$  as a guide to identifying fairly large  $L$  and  $E$  ranges where the sensitivity to the sign of  $\theta_{31}$  is significantly large. As an example,  $P^\mu$  and  $P_e^\mu$  combine constructively in the range 5–10 GeV and 6000–9700 Km to yield a potentially large signal (4) for matter effect for  $\theta_{31} > 0$ . We also identify regions where an appreciable sensitivity to  $\theta_{13}$  exists.

## References

- [1] Kamiookande collaboration, Y. Fukuda et al., Atmospheric  $\nu_e/\nu_\mu$  ratio in the multi-GeV energy range, Phys. Lett. B 335, 237 (1994).
- [2] Super-Kamiookande collaboration, Y. Fukuda et al., Evidence for oscillation of atmospheric neutrinos, Phys. Rev. Lett. 81, 1562 (1998) [hep-ex/9807003].
- [3] Super-Kamiookande collaboration, Y. Fukuda et al., Measurement of the flux and zenith-angle distribution of upward through-going muons by Super-Kamiookande, Phys. Rev. Lett. 82, 2644 (1999) [hep-ex/9812014].
- [4] E. Kearns, Atmospheric neutrino results from SuperKamiookande, talk at XX Ist International Conference on Neutrino Physics and Astrophysics (Neutrino-2004), Paris, June 14-19, 2004, see <http://neutrino2004.in2p3.fr/>
- [5] MACRO collaboration, M. Ambrosio et al., Atmospheric neutrino oscillations from upward throughgoing muon multiple scattering in MACRO, Phys. Lett. B 566, 35 (2003) [hep-ex/0304037];  
MACRO collaboration, M. Ambrosio et al., Measurements of atmospheric muon neutrino oscillations, global analysis of the data collected with MACRO detector, Eur. Phys. J. C 36, 323 (2004).
- [6] Soudan-2 collaboration, W. W. M. Allison et al., The atmospheric neutrino flavor ratio from a 3.9 ducial kiloton-year exposure of Soudan 2, Phys. Lett. B 449, 137 (1999) [hep-ex/9901024].
- [7] R. Becker-Szendy et al., Neutrino measurements with the IMB detector, Nucl. Phys. Proc. Suppl. 38, 331 (1995).

- [8] K2K collaboration, M. H. Ahn et al., Indications of neutrino oscillation in a 250-Km long-baseline experiment, *Phys. Rev. Lett.* 90, 041801 (2003) [[hep-ex/0212007](#)].
- [9] C. Cattadori, Results from radiochemical solar neutrino experiments, talk at XX Ist International Conference on Neutrino Physics and Astrophysics (Neutrino-2004), Paris, June 14-19, 2004, see <http://neutrino2004.in2p3.fr/>
- [10] B. T. Cleveland et al., Measurement of the solar electron neutrino flux with the Homestake chlorine detector, *Astrophys. J.* 496, 505 (1998).
- [11] V. Gavrin, Results from the Russian American gallium experiment (SAGE), talk at VIIth International conference on Topics in Astroparticle and Underground Physics (TAUP03), Seattle, Sept. 5-9, 2003;  
SAGE collaboration, J. N. Abdurashitov et al., Measurement of the solar neutrino capture rate by the Russian-American gallium solar neutrino experiment during one half of the 22-year cycle of solar activity, *J. Exp. Theor. Phys.* 95, 181 (2002) [*Zh. Eksp. Teor. Fiz.* 122, 211 (2002)] [[astro-ph/0204245](#)].
- [12] GALLEX collaboration, W. Hampel et al., GALLEX solar neutrino observations: Results for GALLEX IV, *Phys. Lett. B* 447, 127 (1999).
- [13] E. Bellotti, The Gallium Neutrino Observatory (GNO), talk at VIIth International conference on Topics in Astroparticle and Underground Physics (TAUP03), Seattle, Sept. 5-9, 2003;  
GNO collaboration, M. Altmann et al., GNO solar neutrino observations: Results for GNO I, *Phys. Lett. B* 490, 16 (2000) [[hep-ex/0006034](#)].
- [14] Super-Kamiokande collaboration, S. Fukuda et al., Determination of solar neutrino oscillation parameters using 1496 days of Super-Kamiokande-I data, *Phys. Lett. B* 539, 179 (2002) [[hep-ex/0205075](#)].
- [15] SNO collaboration, Q. R. Ahmad et al., Direct evidence for neutrino flavor transformation from neutral-current interactions in the Sudbury Neutrino Observatory, *Phys. Rev. Lett.* 89, 011301 (2002) [[nucl-ex/0204008](#)].
- [16] SNO collaboration, S. N. Ahmed et al., Measurement of the total active B-8 solar neutrino flux at the Sudbury Neutrino Observatory with enhanced neutral current sensitivity, *Phys. Rev. Lett.* 92, 181301 (2004) [[nucl-ex/0309004](#)].
- [17] KamLAND collaboration, T. Araki et al., Measurement of neutrino oscillation with KamLAND: Evidence of spectral distortion, [hep-ex/0406035](#);  
KamLAND collaboration, K. Eguchi et al., First results from KamLAND: Evidence for reactor antineutrino disappearance, *Phys. Rev. Lett.* 90, 021802 (2003) [[hep-ex/0212021](#)].
- [18] L. Wolfenstein, Neutrino Oscillations In Matter, *Phys. Rev. D* 17, 2369 (1978);

- S. P. Mikheev and A. Y. Smirnov, Resonance Enhancement of Oscillations in Matter and Solar Neutrino Spectroscopy, *Sov. J. Nucl. Phys.* 42, 913 (1985) [*Ad. Fiz.* 42, 1441 (1985)].
- [19] S. Goswami, Global analysis of neutrino oscillation, talk at XX Ist International Conference on Neutrino Physics and Astrophysics (Neutrino-2004), Paris, June 14-19, 2004, see <http://neutrino2004.in2p3.fr/>, [hep-ph/0409224].
- [20] J. N. Bahcall, M. C. Gonzalez-Garcia and C. Pena-Garay, Solar neutrinos before and after Neutrino 2004, *JHEP* 0408, 016 (2004) [hep-ph/0406294].
- [21] M. Maltoni, T. Schwetz, M. A. Tortola and J. W. F. Valle, Status of global fits to neutrino oscillations, [hep-ph/0405172].
- [22] M. C. Gonzalez-Garcia, Global analysis of neutrino data, [hep-ph/0410030].
- [23] P. Huber, M. Lindner, M. Rolinec, T. Schwetz and W. Winter, Prospects of accelerator and reactor neutrino oscillation experiments for the coming ten years, [hep-ph/0403068].
- [24] M. Diwan, NuM I CONF-GEN 886, and The MINOS Technical Design Report, NuM I-L-337, Oct 1998.
- [25] ICARUS collaboration, P. Aprili et al., The ICARUS experiment: A second-generation proton decay experiment and neutrino observatory at the Gran Sasso laboratory. Cloning of T600 modules to reach the design sensitive mass. (Addendum), CERN-SPSC-2002-027
- [26] OPERA collaboration, D. Duchesneau, The CERN - Gran Sasso neutrino program, eConf C0209101, TH09 (2002) [*Nucl. Phys. Proc. Suppl.* 123, 279 (2003)] [hep-ex/0209082]
- [27] Y. Itow et al., The JHF-Kamioka neutrino project, [hep-ex/0106019].
- [28] Nova collaboration, D. Ayres et al., Letter of intent to build an off-axis detector to study  $\theta_{13}$  oscillations with the NuMI neutrino beam, [hep-ex/0210005].
- [29] H. Minakata, H. Sugiyama, O. Yasuda, K. Inoue and F. Suekane, Reactor measurement of  $\theta_{13}$  and its complementarity to long-baseline experiments, *Phys. Rev. D* 68, 033017 (2003) [hep-ph/0211111].
- [30] M. H. Shaevitz and J. M. Link, Using reactors to measure  $\theta_{13}$ , [hep-ex/0306031].
- [31] L. Oberauer,  $\theta_{13}$  measurements with reactors, talk at XX Ist International Conference on Neutrino Physics and Astrophysics (Neutrino-2004), Paris, June 14-19, 2004, see <http://neutrino2004.in2p3.fr/>
- [32] Chooz collaboration, M. Apollonio et al., Limits on neutrino oscillations from the CHOOZ experiment, *Phys. Lett. B* 466, 415 (1999) [hep-ex/9907037].

- [33] Chooz collaboration, M. Apollonio et al., Search for neutrino oscillations on a long base-line at the CHOOZ nuclear power station, *Eur. Phys. J. C* 27, 331 (2003) [[hep-ex/0301017](#)].
- [34] T. Lasserre,  $\theta_{13}$  measurement with the Double-Chooz experiment, talk at The 5th workshop on Neutrino Oscillations and their Origin, see <http://www-sk.icrr.u-tokyo.ac.jp/noon2004/>
- [35] H. Gallagher, Other (past, present and future) atmospheric neutrino experiments, talk at XX Ist International Conference on Neutrino Physics and Astrophysics (Neutrino-2004), Paris, June 14-19, 2004, see <http://neutrino2004.in2p3.fr/>.
- [36] A. Yu. Smirnov, Summary of NOON 2004, talk at The 5th workshop on Neutrino Oscillations and their Origin, see <http://www-sk.icrr.u-tokyo.ac.jp/noon2004/>
- [37] C. Albright et al., Physics at a neutrino factory, [[hep-ex/0008064](#)].
- [38] R. Gandhi, P. Ghoshal, S. Goswami, P. Mehta and S. U. Sankar, Large matter effects in  $\nu_{\mu} \rightarrow \nu_{\tau}$  oscillations, [[hep-ph/0408361](#)].
- [39] M. C. Banuls, G. Barenboim and J. Bernabeu, Medium effects for terrestrial and atmospheric neutrino oscillations, *Phys. Lett. B* 513, 391 (2001) [[hep-ph/0102184](#)].
- [40] T. Tabarelli de Fatis, Prospects of measuring  $\sin^2 2\theta_{13}$  and the sign of  $\delta m^2$  with a massive magnetized detector for atmospheric neutrinos, *Eur. Phys. J. C* 24, 43 (2002) [[hep-ph/0202232](#)].
- [41] S. Palomares-Ruiz and S. T. Petcov, Three-neutrino oscillations of atmospheric neutrinos,  $\theta_{13}$ , neutrino mass hierarchy and iron magnetized detectors, [[hep-ph/0406096](#)].
- [42] D. Indumathi and M. V. N. Murthy, A question of hierarchy: Matter effects with atmospheric neutrinos and anti-neutrinos, [[hep-ph/0407336](#)].
- [43] R. Gandhi, P. Mehta and S. Uma Sankar, Matter effects in atmospheric  $\nu_{\mu} \rightarrow \nu_{\tau}$  events, A note prepared for solar and atmospheric working group of American Physical Society, HRIP-04-10-001.
- [44] M. Diwan et al., Very long baseline neutrino oscillation experiment for precise determination of oscillation parameters and search for  $\nu_{\mu} \rightarrow \nu_{\tau}$  appearance and CP violation. (F), [[hep-ex/0211001](#)];  
M. V. Diwan et al., Very long baseline neutrino oscillation experiments for precise measurements of mixing parameters and CP violating effects, *Phys. Rev. D* 68, 012002 (2003) [[hep-ph/0303081](#)].
- [45] F. DeJongh, Long baseline neutrino physics: From Fermilab to Kamioka, *Fermilab. Pub. 02*, 033 E [[hep-ex/0203005](#)].

- [46] S. M. Bilenky, Neutrino Oscillations And Neutrino Mixing. (In Russian), *Fiz. Elem. Chast. Atom. Yadra* 18, 449 (1987);  
S. M. Bilenky and S. T. Petcov, Massive Neutrinos And Neutrino Oscillations, *Rev. Mod. Phys.* 59, 671 (1987) [Erratum *ibid.* 61, 169 (1989)].
- [47] V. D. Barger, K. Whisnant, S. Pakvasa and R. J. N. Phillips, Matter Effects On Three-Neutrino Oscillations, *Phys. Rev. D* 22, 2718 (1980).
- [48] C. W. Kim, W. K. Sze and S. Nussinov, On Neutrino Oscillations And The Landau-Zener Formula, *Phys. Rev. D* 35, 4014 (1987).
- [49] H. W. Zaglauer and K. H. Schwarzer, The Mixing Angles In Matter For Three Generations Of Neutrinos And The MSW Mechanism, *Z. Phys. C* 40, 273 (1988).
- [50] T. Ohlsson and H. Snellman, Three flavor neutrino oscillations in matter, *J. Math. Phys.* 41, 2768 (2000) [Erratum *ibid.* 42, 2345 (2001)] [hep-ph/9910546]. T. Ohlsson and H. Snellman, Neutrino oscillations with three flavors in matter: Applications to neutrinos traversing the earth, *Phys. Lett. B* 474, 153 (2000) [Erratum *ibid.* 480, 419 (2000)] [hep-ph/9912295].
- [51] Z. Z. Xing, New formulation of matter effects on neutrino mixing and CP violation, *Phys. Lett. B* 487, 327 (2000) [hep-ph/0002246].
- [52] T. Ohlsson, Neutrino oscillations in matter and their applications, *Phys. Scripta T* 93, 18 (2001).
- [53] B. Brahmachari, S. Choubey and P. Roy, CP violation and matter effect for a variable earth density in very long baseline experiments, *Nucl. Phys. B* 671, 483 (2003) [arXiv:hep-ph/0303078].
- [54] T. Ota and J. Sato, Matter profile effect in neutrino factory, *Phys. Rev. D* 63, 093004 (2001) [arXiv:hep-ph/0011234].
- [55] K. Kinoshita, A. Takamura and H. Yokoyama, Exact formula of probability and CP violation for neutrino oscillations in matter, *Phys. Lett. B* 537, 86 (2002) [hep-ph/0203099];  
K. Kinoshita, A. Takamura and H. Yokoyama, All you ever want to know about neutrino oscillation probabilities in constant matter, *Phys. Rev. D* 66, 073005 (2002) [hep-ph/0205295].
- [56] P. F. Harrison, W. G. Scott and T. J. Weiler, Exact matter-covariant formulation of neutrino oscillation probabilities, *Phys. Lett. B* 565, 159 (2003) [hep-ph/0305175].
- [57] E. K. Akhmedov, R. Johansson, M. Lindner, T. Ohlsson and T. Schwetz, Series expansions for three-flavor neutrino oscillation probabilities in matter, *JHEP* 0404, 078 (2004)

- [58] A. M. Dziewonski and D. L. Anderson, *Phys. Earth Planet. Int.* 25, 297 (1981); see [http://solid\\_earth.ou.edu/prem.html](http://solid_earth.ou.edu/prem.html);  
We use the parametrization given in R. Gandhi, C. Quigg, M. H. Reno and I. Sarcevic, *Ultrahigh-energy neutrino interactions, Astropart. Phys.* 5, 81 (1996). [[hep-ph/9512364](#)].
- [59] See for e.g. I. Mocioiu and R. Shrock, *Phys. Rev. D* 62, 053017 (2000); *ibid.* *JHEP* 0111, 050 (2001) [[hep-ph/0106139](#)].
- [60] V. D. Barger, S. Geer, R. Raju and K. Whisnant, Long-baseline study of the leading neutrino oscillation at a neutrino factory, *Phys. Rev. D* 62, 013004 (2000); [[hep-ph/9911524](#)]; Determination of the pattern of neutrino masses at a neutrino factory, *Phys. Lett. B* 485, 379 (2000) [[hep-ph/0004208](#)].
- [61] M. Lindner, The physics potential of future long baseline neutrino oscillation experiments. ((G)), *Nucl. Phys. Proc. Suppl.* 118, 199 (2003) [[hep-ph/0210377](#)];  
M. Lindner, The physics potential of future long-baseline neutrino oscillation experiments, *Springer Tracts Mod. Phys.* 190, 209 (2003) [[hep-ph/0209083](#)].
- [62] V. Barger, D. Marfatia and K. Whisnant, Breaking eight-fold degeneracies in neutrino CP violation, mixing, and mass hierarchy, *Phys. Rev. D* 65, 073023 (2002) [[hep-ph/0112119](#)];  
V. Barger, D. Marfatia and K. Whisnant, O<sub>3</sub>-axis beams and detector clusters: Resolving neutrino parameter degeneracies, *Phys. Rev. D* 66, 053007 (2002) [[hep-ph/0206038](#)].
- [63] H. Minakata and H. Nunokawa, Exploring neutrino mixing with low energy superbeams, *JHEP* 0110, 001 (2001) [[hep-ph/0108085](#)];  
H. Minakata, H. Nunokawa and S. J. Parke, Parameter degeneracies in neutrino oscillation measurement of leptonic CP and T violation, *Phys. Rev. D* 66, 093012 (2002) [[hep-ph/0208163](#)].
- [64] O. Yasuda, New plots and parameter degeneracies in neutrino oscillations, [[hep-ph/0405005](#)].
- [65] A. Cervera, A. Donini, M. B. Gavela, J. J. Gomez Cadenas, P. Hernandez, O. Mena and S. Rigolin, Golden measurements at a neutrino factory, *Nucl. Phys. B* 579, 17 (2000) [Erratum *ibid.* B 593, 731 (2001)] [[hep-ph/0002108](#)].
- [66] A. Donini, D. Meloni and P. Migliozzi, The silver channel at the neutrino factory, *Nucl. Phys. B* 646, 321 (2002) [[hep-ph/0206034](#)].
- [67] P. Huber and W. Winter, Neutrino factories and the 'magic' baseline, *Phys. Rev. D* 68, 037301 (2003) [[hep-ph/0301257](#)].
- [68] R. Gandhi, P. Ghoshal, S. Goswami, P. Mehta and S. Uma Sankar, work in progress.

- [69] E. K. Akhmedov, A. Dighe, P. Lipari, A. Y. Smirnov, Atmospheric neutrinos at Super-Kamiokande and parametric resonance in neutrino oscillations, *Nucl. Phys. B* 542, 3 (1999) [[hep-ph/9808270](#)];  
 J. Bernabeu, S. Palmares-Ruiz, A. Perez, S. T. Petcov, The earth mantle-core effect in charge-asymmetries for atmospheric neutrino oscillations, *Phys. Lett. B* 531, 90 (2002) [[hep-ph/0110071](#)].
- [70] Tests of CPT using atmospheric neutrinos in such a detector have been discussed in A. Datta, R. Gandhi, P. Mehta and S. Uma Sankar, Atmospheric Neutrinos as a probe of CPT and Lorentz Violation, *Phys. Lett. B* 597, 356-361 (2004) [[hep-ph/0312027](#)].
- [71] D. Choudhury and A. Datta, Detecting matter effects in long baseline experiments, [[hep-ph/0410266](#)].
- [72] S. Choubey and P. Roy, Testing maximality in muon neutrino flavor mixing, *Phys. Rev. Lett.* 93, 021803 (2004) [[hep-ph/0310316](#)].
- [73] V. Agrawal, T. K. Gaisser, P. Lipari and T. Stanev, Atmospheric neutrino flux above 1 GeV, *Phys. Rev. D* 53, 1314 (1996) [[hep-ph/9509423](#)].
- [74] N. Y. Agafonova et al. [MONOLITH Collaboration], LNGS-P26-2000; <http://castore.mi.infn.it/monolith/>
- [75] See <http://www.insc.res.in/ino>.